Black-hole masses, accretion rates and hot- and cold-mode accretion in radio galaxies at $z \sim 1$

C. A. C. Fernandes[1,2,3,4⋆], M. J. Jarvis[4,5], A. Martínez-Sansigre[6], S. Rawlings[4], J. Afonso[2,3], M.J. Hardcastle[7], M. Lacy[8], J. A. Stevens[7], and E. Vardoulaki[4,9]

[1] *Observatório Nacional, Rua General José Cristino, 77, 20921-400, Rio de Janeiro -RJ, Brazil*
[2] *Observatório Astronómico de Lisboa, Faculdade de Ciências, Universidade de Lisboa, Tapada da Ajuda, 1349-018 Lisbon, Portugal*
[3] *Centro de Astronomia e Astrofísica da Universidade de Lisboa, Lisbon, Portugal*
[4] *University of Oxford, Subdepartment of Astrophysics, Denys Wilkinson Building, Keble Road, Oxford OX1 2DL, UK*
[5] *Department of Physics, University of the Western Cape, Private Bag X17, Bellville 7535, South Africa*
[6] *Institute of Cosmology and Gravitation, University of Portsmouth, Dennis Sciama Building, Burnaby Road, Portsmouth, PO1 3FX, UK*
[7] *Centre for Astrophysics Research, STRI, University of Hertfordshire,Hatfield, AL10 9AB, UK*
[8] *National Radio Astronomy Observatory, 520 Edgemont Road, Charlottesville, VA 22903, USA*
[9] *Department of Physics, University of Crete, GR-71003, Heraklion, Greece*

ABSTRACT

Understanding the evolution of accretion activity is fundamental to our understanding of how galaxies form and evolve over the history of the Universe. We analyse a complete sample of 27 radio galaxies which includes both high-excitation (HEGs) and low excitation galaxies (LEGs), spanning a narrow redshift range of $0.9 < z < 1.1$ and covering a factor of ~ 1000 in radio luminosity. Using data from the *Spitzer Space Telescope* combined with ground-based optical and near-infrared imaging, we show that the host galaxies have masses in the range of $10.7 < \log_{10}(M/M_\odot) < 12.0$ with HEGs and LEGs exhibiting no difference in their mass distributions. We also find that HEGs accrete at significantly higher rates than LEGs, with the HEG/LEG division lying at an Eddington ratio of $\lambda \sim 0.04$, which is in excellent agreement with theoretical predictions of where the accretion rate becomes radiatively inefficient, thus supporting the idea of HEGs and LEGs being powered by different modes of accretion. Our study also shows that at least up to $L_{151\mathrm{MHz}} \sim 3 \times 10^{27}\,\mathrm{W\,Hz^{-1}\,sr^{-1}}$, HEGs and LEGs are indistinguishable in terms of their radio properties. From this result we infer that, at least for the lower radio luminosity range, another factor besides accretion rate must play an important role in the process of triggering jet activity.

Key words: galaxies: active - galaxies: jets - infrared: galaxies - radio continuum: galaxies - quasars: general - galaxies : nuclei

1 INTRODUCTION

It is now widely accepted that black holes reside in the centre of nearly all galaxies (e.g. Begelman & Rees 1996; Richstone et al. 1998; Magorrian et al. 1998). Accretion onto these black holes is believed to be the mechanism responsible for powering Active Galactic Nuclei (AGN; e.g. Antonucci 1993; Urry & Padovani 1995).

The black holes in these galaxies can accrete matter, either from the interstellar medium close to the event horizon or from thick disks of gas. In order to be accreted, gas needs to fall in with an angular momentum that does not exceed that needed for disk capture. In the vicinity of the sphere of influence of the black hole, the Keple-

rian motion of the accreting material is exceedingly high, thus processes that redistribute the angular momentum of the accreting gas determine the accretion rate. Galactic mergers, gravitational torques from bars and other structures can efficiently channel gas into the nuclear regions (e.g. Shlosman et al. 1989, 1990; Hernquist & Mihos 1995). Closer to the sphere of influence of the black hole, however, other mechanisms, such as turbulence driven by magnetic instabilities, are efficient sources of angular momentum transport (e.g. Matsumoto & Tajima 1995; Stone et al. 1996).

There are different modes of accretion. The 'standard' accretion mode occurs when matter is accreted onto the black hole through a radiatively efficient process. This is generally associated with optically thick and geometrically thin accretion disks (e.g. Shakura & Sunyaev 1973), and thought to be associated with quasar activity. This process is likely

⋆ E-mail: cfernandes@on.br

to be prevalent where there is a plentiful supply of cold gas, which can accrete efficiently towards the black hole, and as such the fuel, in the form of the cold gas, should also be able to condense and provide the fuel for star formation (e.g. Hardcastle et al. 2007). Indirect evidence for such a scenario comes from the similar evolution of the AGN activity in the Universe and the star-formation rate density, both increasing rapidly from $z \sim 0 \rightarrow 1$ and steadily turning over at $z > 3$ (e.g. Silverman et al. 2009). Furthermore, such a close connection between AGN and star-formation activity may provide a relatively straightforward explanation of the local correlation between galaxy mass and black-hole mass (Magorrian et al. 1998; Ferrarese & Merritt 2000; Gebhardt et al. 2000; Häring & Rix 2004).

Accretion in an AGN may also be radiatively inefficient. When mass accretion is too low ($\dot{M} \ll \dot{M}_{\rm Edd}$), the inflowing gas may not be able to radiate the gravitational potential energy liberated due to accretion. Magnetohydrodynamic simulations show that the energy dissipated during accretion could heat up only the ions in the disk (e.g. Quataert & Gruzinov 1999; Medvedev 2000; Quataert et al. 2002). On the other hand, radiative losses, synchrotron radiation, and Comptonization of low-energy photons take energy from the electrons, cooling them. The characteristic time-scale for the hot ions and the cold electrons to achieve thermal equilibrium through coupling depends on the gas temperature in the vicinity of the black hole, and is inversely proportional to the number density of ions. When the accretion rate is low, the ionic density is also small, and this time-scale is of the same order as, or larger than, the inflow time. Thus a two-temperature plasma is expected to form when $\dot{M} \ll \dot{M}_{\rm Edd}$. In this regime, advection dominated accretion flows (ADAFs) can be formed. This radiatively inefficient process is currently taken as the most likely explanation for accretion flows around black holes at low accretion rates. The critical accretion rate below which it becomes radiatively inefficient is estimated to be $\dot{M}_{\rm crit} \simeq \alpha^2 \dot{M}_{\rm Edd}$ (Narayan & Yi 1995), where α is a dimensionless parameter that measures the efficiency of angular momentum transport in disks. With the standard value of $\alpha = 0.25$ (e.g. Esin et al. 1997), the critical accretion rate is situated around $\dot{M}_{\rm crit} \sim 0.06$ normalised to the Eddington accretion rate. Due to the inability of the gas to cool down radiatively in this regime, the gas can be driven to a higher temperature, and thus cause a vertical thickening of the disk. ADAFs are thus thought to be characteristic of hot thick disks.

What causes the different modes of radiatively efficient and inefficient accretion remains uncertain. It has been suggested that the nature of the gas being accreted might determine the type of accretion, with cold gas producing a stable accretion disk and thus a radiatively efficient accretion, and hot gas producing flows that would result in an ADAF (e.g. Hardcastle et al. 2007). The black hole spin has also been suggested to play a role in determining the accretion mode (e.g. Martínez-Sansigre & Rawlings 2011).

Radio galaxies are a class of AGN that can be divided into two sub-categories according to the ratio between the intensity of high and low excitation emission lines in their optical spectra: low excitation galaxies (LEGs) and high excitation galaxies (HEGs). The two distinct classes were first noted by Hine & Longair (1979) and further cat-

egorised by Laing et al. (1994) and Jackson & Rawlings (1997). Jackson & Rawlings (1997) defined LEGs as objects that obey the following requirements: have [OIII]-line equivalent widths < 10Å, have a ratio [OII]/[OIII] > 1, or both.

It is widely accepted that LEGs could be the result of radiatively inefficient accretion processes (e.g. Hardcastle et al. 2007; Buttiglione et al. 2010; Mingo et al. 2014). Best & Heckman (2012) compared a large number of local radio-loud AGN and concluded that the HEG and LEG populations show different accretion rate distributions, consistent with the idea that radiative efficiency is determined purely on accretion rate.

This is a subject that impacts on the most relevant issues for models of AGN and their roles in galaxy evolution. For instance, if the HEG/LEG distinction is indeed related to the accretion process, then the fact that their radio properties are similar requires that the power being channeled into the jets is independent of the accretion rate.

Moreover, given that radiatively efficient accretion is related to the 'quasar mode' form of feedback processes in AGN, and radiatively inefficient accretion associated with 'radio mode' AGN feedback in semi-analytic models (e.g. Croton et al. 2006), the HEG and LEG characterisation could be used to diagnose the different modes at play in each system. LEGs would for instance be the perfect laboratories to investigate the 'radio mode' form of feedback, currently taken as being the principal mechanism responsible for shutting down star formation in the most massive systems at $z < 1$.

In this paper we investigate the HEG/LEG division in radio-loud sources and their different accretion processes, extending the study of Best & Heckman (2012) to high-redshift sources ($z \sim 1$). Moving to high redshift is not only complementary in terms of looking back time but also in terms of luminosity as it provides us with the opportunity to study the rarer more luminous objects in each class.

Section 2 describes the data selection. Section 3 describes the SED fitting method used. In Section 4 and 5 the SED fits are shown and the physical values extracted from them are presented. The results are discussed in Section 6, and conclusions are presented in Section 7. Throughout this paper we adopt the following values for the cosmological parameters: $H_0 = 70 \, {\rm km \, s^{-1} \, Mpc^{-1}}$, $\Omega_{\rm M} = 0.3$ and $\Omega_{\Lambda} = 0.7$.

2   DATA

We use *Spitzer Space Telescope* observations and multiple data collected from the literature, ranging from mid-infrared to optical wavelengths, of the sample of radio galaxies presented by Fernandes et al. (2011). This sample consists of 27 radio sources selected from the spectroscopically complete 3CRR (Laing et al. 1983), 6CE (Eales et al. 1997; Rawlings et al. 2001), 6C* (Jarvis et al. 2001a,b), 7CRS (Lacy et al. 1999; Willott et al. 2003) and TOOT (Hill & Rawlings 2003; Vardoulaki et al. 2010) surveys to have narrow lines and a redshift of $0.9 \lesssim z \lesssim 1.1$. The narrow-line selection was intended to ensure the exclusion of quasars from the sample (though 3C343 has since been classified as a quasar and 3C22 is classified as a weak quasar).

2.1 Spitzer data

The *Spitzer* data consist of observations with MIPS $24\,\mu$m and IRAC 3.6, 4.5, 5.8 and $8.0\,\mu$m bands. The MIPS and IRAC observations took place in August 2006 and August 2007, as described by Fernandes et al. (2011). The photometric measurements for the IRAC data were performed using a 7 arcsec diameter aperture with aperture corrections of 1.112, 1.113, 1.125 and 1.218 for IRAC channels 1, 2, 3 and 4 respectively, unless there was a nearby source in which case we used a 3.5 arcsec diameter aperture with appropriate aperture corrections. For MIPS we extracted the photometry in a 13 arcsec diameter aperture with aperture correction of 1.167. A summary of these data is shown in Table 1.

2.2 Literature data

To increase the number of data points in the near-infrared and optical bands, we used as many photometric values as possible from the literature. The values available were extracted with a range of different apertures and, where possible, we chose apertures of 8 arcsec, or larger, which approximately encompass the whole of the emission from the galaxies in our sample.

2.2.1 Aperture corrections

For consistency, when magnitude values were only available with smaller apertures we applied a correction to transform them into magnitudes with a 8 arcsec aperture or larger. Given that the majority of the photometric data in the literature is presented in apertures of 8 or 9 arcsec diameter, and that this is a good approximation to the total flux of the source, we preferred to convert all the smaller aperture magnitudes to their equivalent value at 8 or 9 arcsec.

All the magnitudes measured using smaller apertures that we converted to 8 or 9 arcsec were measured either in 4 or 5 arcsec apertures, thus the corrections are small (e.g. Bryant et al. 2009). To find relations between 4 and 5 arcsec and 8 or 9 arcsec, we gathered a large sample of galaxies (~ 40 galaxies), from the papers referenced in Tables 1 to 4 of the Appendix, which had photometry available for several different apertures. With this sample, we computed linear relations between the magnitudes at 4 arcsec and 9 arcsec and between 5 arcsec and 8 arcsec. We then used these linear fits to determine all magnitudes in 8 or 9 arcsec apertures.

We also applied a Galactic extinction correction to all the magnitude values that had not been corrected based on the maps of Schlegel et al. (1998).

2.2.2 Line emission correction

Following Jarvis et al. (2001b) we also subtracted the flux of the dominant emission lines Hα, [OII], [NeV], MgII, [NeIV] and CII], from J, R, F702W, F606W, V, B, and g bands, as these lines can contribute a significant percentage to the total flux of the band where they lie. Where the line fluxes were not available we used the [OII] fluxes from Fernandes et al. (2011) and determined the remaining emission lines using the line ratios given by McCarthy (1993) and Best et al.

(1997). When the flux of Hα is not known, we used the average ratio estimated by McCarthy (1993) for high redshift radio galaxies ($z \lesssim 2$) from the 3CR survey.

To correct for emission line contamination we then determined the location of each emission line for the redshift of the given source and account for the shape of the filter at that wavelength. Given the uncertainties affecting the aperture, emission-line contamination and Galactic extinction corrections, we assume an additional 10 per cent error in the flux density for each magnitude value that had any of these corrections applied. All these corrections are detailed in Tables 1, 2 3, and 4 of the Appendix.

3 SED FITTING

The photometric data span a wavelength range from $0.36\,\mu$m to $24\,\mu$m. At optical wavelengths, the emission from radio galaxies - obscured AGN - is dominated by the stellar emission of the host galaxy. At mid-infrared wavelengths, dust in the 'torus' region that re-emits the radiation from the central AGN is the main source of emission, at least for those sources with a relatively powerful and radiatively efficient AGN. This can be thought of as a composite of the central emission passing through a screen of dust. We follow the approach of Martínez-Sansigre et al. (2007, 2009) and model the radio galaxies with a galaxy template that dominates the emission in the optical part of the spectrum and a quasar template, extinguished by a dust extinction law, to fit the emission in the infrared spectral region.

3.1 Galaxy template

To replicate the host galaxy emission, we consider a Bruzual and Charlot stellar synthesis model (Bruzual & Charlot 2003, hereafter BC03), as well as the Maraston et al. fuel-consumption stellar population synthesis model (Maraston 2005, hereafter M05). For both of these we assume a Salpeter initial mass function and solar metallicity.

Since radio galaxies are almost exclusively hosted by elliptical galaxies or recent merger remnants (e.g. Dunlop et al. 2003; Floyd et al. 2010), we expect them to have a strong short episode of star formation in the beginning of their formation and for the star formation rate to quickly drop subsequently. Therefore, we consider that a single simple stellar population suffices to reproduce the host galaxy's star formation history, and a synthesis of SSPs is not required. To select the stellar age of our template we note that our objects all have $z \sim 1$, when, according to the adopted cosmology, the Universe was $\sim 5.7\,$Gyr old. We, thus, constrain the range of possible ages with an upper limit for the stellar population age of 6 Gyr. As for a lower limit, previous studies have shown that for passively-evolving early-type galaxies in cluster environments, the bulk of stars form at $z \gtrsim 3$ and in low-density environments at $z \gtrsim 1.5 - 2$ (e.g. Bower et al. 1992, 1998; Renzini 2006). This yields a stellar age of $\sim 5.6\,$Gyr for cluster environments and $\sim 1.5 - 2.5\,$Gyr for field galaxies. Even though our sample consists of powerful radio galaxies, which tend to inhabit high-density environments as suggested by various lines of observations (e.g. Hill & Lilly 1991; Wold et al. 2001; Hardcastle 2004; Kauffmann et al. 2008; Falder et al.

Table 1. *Spitzer* photometry for our sample of radio galaxies. **Column 1** gives the name of the object; **Columns 2, 4, 6, 8, 10** give the flux density at 3.6, 4.5, 5.8, 8.0 and 24 μm, respectively; **Columns 3, 5, 7, 9, 11** give the respective flux density errors.

Object	$S_{3.6\,\mu m}$ μJy	$\mathrm{Err}_{S_{3.6\,\mu m}}$ μJy	$S_{4.5\,\mu m}$ μJy	$\mathrm{Err}_{S_{4.5\,\mu m}}$ μJy	$S_{5.8\,\mu m}$ μJy	$\mathrm{Err}_{S_{5.8\,\mu m}}$ μJy	$S_{8.0\,\mu m}$ μJy	$\mathrm{Err}_{S_{8.0\,\mu m}}$ μJy	$S_{24\,\mu m}$ μJy	$\mathrm{Err}_{S_{24\,\mu m}}$ μJy
3C280	277.26	38.69	524.69	87.58	1004.40	126.74	2200.45	204.88	9229.46	258.67
3C268.1	35.45	13.94	78.20	33.91	108.84	43.09	209.22	64.37	940.96	123.57
3C356	108.00	11.00	110.00	11.00	122.00	14.00	434.00	47.00	4060.00	192.00
3C184	129.88	44.40	145.48	46.09	242.00	55.00	288.00	76.00	742.00	184.00
3C175.1	119.60	25.54	109.55	40.21	92.03	42.56	124.70	53.55	836.90	166.56
3C22	1399.41	86.86	2431.72	188.43	3647.24	239.86	5852.97	333.61	13744.13	310.40
3C289	38.91	14.62	44.00	25.53	26.81	25.20	37.15	26.55	3650.16	168.21
3C343	151.35	28.62	142.75	45.74	211.85	60.29	683.25	114.58	7294.40	230.19
6CE1256+3648	62.50	18.44	61.01	29.99	55.72	32.24	133.86	52.70	1351.94	124.20
6CE1217+3645	118.37	25.34	120.80	42.11	125.26	51.99	150.98	53.52	313.64	104.94
6CE1017+3712	26.52	12.15	31.88	21.83	43.08	30.52	129.35	53.11	1136.21	131.80
6CE0943+3958	72.68	19.90	87.66	35.95	141.66	49.31	244.95	70.77	1996.79	153.62
6CE1257+3633	81.58	21.05	70.04	32.11	36.46	27.63	110.35	48.18	850.67	108.30
6CE1019+3924	159.69	29.41	117.47	41.57	75.93	38.14	23.26	28.80	334.56	181.18
6CE1011+3632	74.20	20.11	79.07	34.14	89.07	40.89	200.03	64.69	1326.94	150.39
6CE1129+3710	81.67	21.08	62.57	30.39	40.67	35.62	72.84	41.39	856.71	119.07
6C*0128+394	85.50	21.58	92.74	36.95	65.62	36.02	74.97	42.26	134.85	86.14
6CE1212+3805	74.06	20.10	61.81	30.24	30.77	31.14	55.14	37.46	257.42	92.98
6C*0133+486	53.85	17.20	64.35	30.86	50.99	41.43	75.81	37.92	82.15	75.92
5C6.24	111.17	24.57	102.82	38.89	86.34	41.21	118.65	50.69	728.22	119.30
5C7.23	54.77	17.32	48.11	26.75	67.04	35.75	41.12	34.62	623.52	160.69
5C7.82	114.37	24.92	83.15	34.99	45.29	31.63	55.92	37.71	422.33	154.47
5C7.242	123.35	25.87	104.96	39.33	69.57	36.58	41.92	34.64	1994.72	161.08
5C7.17	30.88	13.10	22.64	18.50	56.68	33.88	5.14	22.51	1371.30	176.80
TOOT1267	114.48	24.91	95.55	37.47	88.35	39.65	141.41	53.90	1079.06	121.87
TOOT1140	50.48	16.63	64.88	30.92	47.60	31.18	28.71	28.25	136.24	80.29
TOOT1066	49.37	16.50	35.92	23.09	-3.85	14.10	16.21	22.64	298.16	86.86

2010), including X-ray observations that show X-ray cavities identified with clusters of galaxies to be spatially coincident with non-thermal radio emission from radio-loud AGN (e.g. Fabian et al. 2002, Bîrzan et al. 2004), we adopt a conservative lower limit for the stellar age of ~ 0.5 Gyr. We thus use templates with 0.5 Gyr, 1 Gyr, 2 Gyr, 3 Gyr, 4 Gyr, 5 Gyr, and 6 Gyr of age for the SED fitting of the galaxies in our sample.

3.2 Quasar and dust template

To model the infrared emission of the radio galaxies, we need to account for the dusty torus absorbing the radiation from the central source and re-emitting it at longer wavelengths. This can be done, as an approximation, by assuming that a radio galaxy is equivalent to a quasar with a layer of obscuring dust in front of it, where this layer can have diverse column densities depending on how obscured the galaxy is (e.g. Martínez-Sansigre et al. 2007, 2009). Indeed, Haas et al. (2008) find that they can reproduce a diversity of rest-frame $1.6 - 10\,\mu$m SEDs of radio galaxies by combining various amounts of extinction of AGN light with host galaxy starlight. This representation is consistent with the orientation-dependent unified scheme and it is intended as a simplification only, as a more careful approximation should fully account for radiative transfer effects in a dusty medium (e.g. Nenkova et al. 2008). This approach would, however, imply a large number of free parameters with too few data

points to constrain them, resulting in a high degeneracy, making it difficult to infer physically meaningful quantities. Thus, we build, as a simplification, a composite model of a quasar and a screen of dust.

As a quasar template, we use the radio-quiet quasar SED by Elvis et al. (1994), which was constructed based on the mean energy distribution of a sample of 29 radio-quiet quasars. We normalise this template by forcing the bolometric luminosity to be 1. For this, we used the median value of the B-band luminosity, L_B, which, according to Table 17 of Elvis et al. (1994), should be $L_{bol} = 10.7 L_B$.

More recent works such as Mason et al. (2013) have shown a composite model of a jet, a truncated thin accretion disk and an ADAF to be a good fit for low-luminosity AGNs, and therefore possibly better suited for LEGs. Mason et al. (2013) however report an insufficient IR-emission produced by the truncated thin disk in order to match the observations. Given these issues, we opt to use the model by Elvis et al. (1994) for all the objects in the sample for consistency.

For a dust template, we used the extinction laws derived by Pei (1992), which replicate how the extinction caused by the different types of dust varies with wavelength. These templates are described by the following summation:

$$\frac{A_\lambda}{A_B}(\lambda) = \sum_{i=1}^{6} \frac{a_i}{(\lambda/\lambda_i)^{n_i} + (\lambda/\lambda_i)^{-n_i} + b_i} \qquad (Pei, 1992),$$

(1)

where a_i, b_i and n_i vary for each term and for each dust type (see Table 4 of Pei 1992 for a full description). The six terms involved represent the background, far-ultraviolet and far-infrared extinctions and the 2175 Å, 9.7 μm and 18μm features. For reddened quasars, SMC dust has been found to be appropriate (e.g. Hopkins et al. 2004; Willott 2005), since dust in the host galaxy of high-redshift galaxies tends to have lower metallicity and thus can be better approximated by SMC dust type. However, for more obscured quasars, and in particular for the majority of the objects in our sample, we find that SMC dust does not provide as good a fit as MW dust. This could be explained by the fact that the dust intersecting the line of sight of the central emission in obscured galaxies comes from the inner region due to the galaxy's edge-on orientation, and the central regions of galaxies are usually more metal rich, as there is in general a metallicity gradient in galaxies (e.g. Davies et al. 1993; Carollo & Danziger 1994; Spolaor et al. 2009). Therefore, we adopted a MW dust type for all the galaxies in our sample.

3.3 Method of fitting

We fit our model to the photometric data points by applying an extinction curve to the intrinsic quasar light template and then adding it to the galaxy light model:

$$S_{\nu,\text{model}} = S_{\nu,\text{QSOmodel}} + S_{\nu,\text{GALmodel}}, \qquad (2)$$

with

$$S_{\nu,\text{QSOmodel}} = S_{\nu,\text{QSOtemplate}} \times 10^{-\frac{A_V \times A_\lambda(\lambda)}{2.5}}, \qquad (3)$$

where $S_{\nu,\text{QSOtemplate}}$ is the quasar light template and $S_{\nu,\text{QSOmodel}}$ is the quasar light model already affected by extinction.

To convert the extinction law $\frac{A_\lambda}{A_B}(\lambda)$ to magnitudes (A_λ) we multiply equation (1) by the term $1/R_V + 1$, where R_V is the ratio of total-to-selective extinction defined by the equation:

$$R_V = \frac{A_V}{E_{B-V}}, \qquad (4)$$

where $E_{B-V} = A_B - A_V$ is the colour excess.

We multiply each template by a coefficient which we allow to vary along a range of physically motivated values.

The extinction law is multiplied by the visual extinction coefficient A_V spanning values of $0 < A_V < 400$. The resolution we use to run through these values varies from galaxy to galaxy depending on how precise the fit is, and we make it finer where the dispersion of the fit is smaller, as detailed below.

After multiplying the extinction law in flux units by the transmitted quasar light, we force it to be as close as possible to the 24 μm flux density value. This means we do not allow the bolometric luminosity of the model to vary freely. For each given A_V, it is fixed by the observed flux density at 24 μm. The reasoning for this is to constrain the fit, as we found that without this step, the higher degeneracy of the fits often provided poorer matches to the data in terms of reduced-χ^2.

The galaxy template, $S_{\nu,\text{GALtemplate}}$, is multiplied by a mass normalisation factor, M_{gal}, which we allow to vary

between 10^{10} and 10^{13} M$_\odot$, an interval that comprises the typical values of stellar mass content in early-type galaxies and certainly the masses of the majority of radio galaxies studied to date (e.g. Seymour et al. 2007):

$$S_{\nu,\text{GALmodel}} = \frac{S_{\nu,\text{GALtemplate}}}{M_\odot} \times M_{\text{gal}} \qquad (5)$$

We then perform a grid search in A_V and M_{gal} to obtain the best fit.

Given that the data from the literature were gathered from several different instruments, we opted to use a single set of filter transmission curves: for J, H and K_s bands we used the filters from the Visible and Infrared Survey Telescope for Astronomy (VISTA; see e.g. Jarvis et al. 2013) For the HST F606W, F702W and F814W passbands, we used the respective HST filter response profiles; for U, B, V, R and I bands we used the filters used on the auxiliary-port camera (ACAM) mounted on the William Herschel Telescope (WHT); finally, for the u, g, r, i and z bands, given that most data at these wavelengths were extracted from the SDSS public release, we used the SDSS bandpass filters. For the small number of photometric data points that were not observed with the exact same filters we use, the errors are smaller or of the same order of magnitude as the uncertainties on the data.

Using the filter responses, we evaluate the flux density that the model produces for each band using the following:

$$\nu S_{\nu,\text{model}} = \frac{\int_{\lambda_i}^{\lambda_f} \nu S_{\nu,\text{unfiltered}} \times T(\lambda)d\lambda}{\int_{\lambda_i}^{\lambda_f} T(\lambda)d\lambda}, \qquad (6)$$

where $S_{\nu,\text{unfiltered}}$ is the flux density of the model before it has been convolved with the filter response; $S_{\nu,\text{model}}$ is the flux density of the model after the filter response has been taken into account; λ_i and λ_f are the wavelength where the filter response starts and ends respectively; and $T(\lambda)$ is the filter transmission curve.

To determine the flux $\nu S_{\nu,\text{data}}$ of the data points, we multiply the flux density values by the mean frequency of each band. The mean frequency is determined by computing the effective wavelength of each band, given by:

$$\lambda_{\text{eff}} = \frac{\int_{\lambda i}^{\lambda_f} \lambda T(\lambda)d\lambda}{\int_{\lambda i}^{\lambda_f} T(\lambda)d\lambda}, \qquad (7)$$

and converting it to ν_{eff}.

We determine the χ^2 distribution of each model using,

$$\chi^2(A_V, M_{\text{gal}}) = \sum_n \left(\frac{\nu S_{\nu,\text{model}}(A_V, M_{\text{gal}}) - \nu S_{\nu,\text{data}}}{\sigma} \right)^2, \qquad (8)$$

where n is the number of flux/magnitude data points available, and σ is the error associated with each data point. We repeat this process for all the different stellar models we are considering (ages 0.5, 1, 2, 3, 4, 5, and 6 Gyr for both BC03 and M05 models) and choose the model that has the lowest χ^2 amongst these.

Sources that are detected below a 2σ level in the imaging data are plotted as upper limits at a 2σ level. We use

their measured photometric flux for the SED fitting and place their error bars between zero and the detection limit for the χ^2 evaluation. However, photometric bands for which both the observed flux density and the model are lower than the flux density limit make no contribution to the χ^2.

4   SED FITS

In Table 2 we present the best-fit values for $A_{\rm V}$, $M_{\rm gal}$ and the stellar age of the SSP template, and in Figure 1 we show these best-fit SEDs overlaid on the data.

We note that for several objects (3C289, 6C1019+39, 5C7.17, 6C1011+36, TOOT00_1267, and TOOT00_1066) there is an excess of emission at the highest frequencies of the optical region of the SED that rises above the galaxy template. This is thought to be either due to scattered light from the central AGN or blue light from young stars (see e.g. Herbert et al. 2010, and references therein). This does not adversely impact our fit for the stellar masses however, as the bulk of the stellar mass is traced by the high-mass-to-light-ratio red stars.

To determine the error associated with each normalisation parameter of the best fitting model we marginalised over the free parameters, $A_{\rm V}$ and $M_{\rm gal}$, choosing a uniform (i.e. constant) prior of $0 \leqslant A_{\rm V} \leqslant 400$ and $10.0 \leqslant \log_{10}(M_{\rm gal}) \leqslant 13.0$. We marginalised the free parameters by integrating the likelihood over the full range of one parameter, for instance $M_{\rm gal}$, in order to get the dependence of the total likelihood on the other parameter, $A_{\rm V}$. This then allows us to determine the uncertainty from the likelihood function in relation to $M_{\rm gal}$, by determining the minimal width of the likelihood function that contains 68 per cent of all the likelihood. We then repeat the same procedure to estimate $\sigma_{A_{\rm V}}$.

5   NOTES ON INDIVIDUAL OBJECTS

In this section we provide notes on the individual sources and their best fit model.

3C280 is well fitted with a model with an $A_{\rm V}$ of ~ 19 and a stellar mass of $M_{\rm gal} \simeq 1.6 \times 10^{11}$ M$_\odot$.

3C268.1 lacks optical or near-IR data in the literature. The fit of the stellar mass of the galaxy is thus not well-constrained, and the best-fit value of $M_{\rm gal} \simeq 2.1 \times 10^{10}$ M$_\odot$ is not reliable due to the lack of data points constraining the fit. The SED fit of this galaxy yields a value for visual dust extinction of $A_{\rm V} \simeq 17$.

3C356 has two bright infrared galaxies at $z = 1.079$ coincident with two radio cores, one northern and one southern, approximately 5 arcsec apart from each other. The identification of the nucleus is a matter of debate in the literature (Eales & Rawlings 1990; Rigler et al. 1992; Best et al. 1997, 2000). We assume the northern component to be the identification of the host galaxy and radio jet. We found a model with a high $A_{\rm V}$ of ~ 127 and a stellar mass of $M_{\rm gal} \simeq 4 \times 10^{11}$ M$_\odot$ to be a good fit for the SED of this galaxy.

3C184 is well fit by a model with a stellar mass of $M_{\rm gal} \simeq 6.6 \times 10^{11}$ M$_\odot$.

3C175.1 has a best fit model with a high $A_{\rm V}$ of ~ 123,

with a rather high uncertainty of $\sigma_{A_{\rm V}} = 116.8$, and a stellar mass of $M_{\rm gal} \simeq 3.8 \times 10^{11}$ M$_\odot$.

3C22 is a reddened quasar (Rawlings et al. 1995; Simpson et al. 1999). As expected for this type of object, it is well fit by a model with a low dust extinction, $A_{\rm V} \sim 7$, and the SED is mainly dominated by the quasar light component. We find that SMC-type dust fits the SED of 3C22 as well as the MW type. We chose the MW type template for consistency.

3C289 has a best fit model with a very high $A_{\rm V}$ of ~ 209, and a stellar mass of $M_{\rm gal} \simeq 8.9 \times 10^{11}$ M$_\odot$.

3C343: The best fit model for the SED of 3C343 was found with a visual extinction of $A_{\rm V} \sim 158$ and a stellar mass of $M_{\rm gal} \simeq 4.3 \times 10^{11}$ M$_\odot$.

6C1256+36 has a best fit model with a high $A_{\rm V}$ of ~ 180, and a stellar mass of $M_{\rm gal} = 7.8 \times 10^{11}$ M$_\odot$.

6C1217+36 is well fit by a model with a very low dust extinction, $A_{\rm V} \approx 1$, and the SED is mainly dominated by the galaxy light component, with a mass of $M_{\rm gal} \simeq 2 \times 10^{11}$ M$_\odot$.

6C1017+37 has a best fit model with a high $A_{\rm V}$ of ~ 141, and a stellar mass of $M_{\rm gal} \simeq 4 \times 10^{11}$ M$_\odot$. The 5.8 and 4.5 μm fluxes are not detected at the 2σ level and represent only limits.

6C0943+39 has a best fit model with a visual extinction of $A_{\rm V} \sim 99$, and a stellar mass of $M_{\rm gal} \simeq 1.4 \times 10^{11}$ M$_\odot$.

6C1257+36 has a best fit model with a visual extinction of $A_{\rm V} \sim 112$, and a stellar mass of $M_{\rm gal} = 3.7 \times 10^{11}$ M$_\odot$.

6C1019+39 is not detected at 8.0 μm or 24 μm at the 2σ level, which makes the fit of the quasar template more problematic. A visual extinction of ~ 110 is our preferred model, with a very high associated uncertainty of ~ 125. Despite this, the galaxy is well fit by a template with a stellar mass of 1.6×10^{11} M$_\odot$.

6C1011+36 has a best fit model with $A_{\rm V} \sim 65$, and a stellar mass of $M_{\rm gal} \simeq 1.3 \times 10^{10}$ M$_\odot$. The high flux of the optical data points compared to the galaxy model suggests that these shorter wavelengths might be contaminated by scattered light as discussed in Section 4.

6C1129+37 is not detected at 8.0 and 5.8 μm at a 2σ level. The best fit model is found for $A_{\rm V} \sim 164$ and a stellar mass of $M_{\rm gal} = 1.4 \times 10^{11}$ M$_\odot$.

6C*0128+39 is not detected at 24, 8.0 or 5.8 μm at the 2σ level, which makes the fitting of the quasar light difficult. We find the best fit quasar model to converge to an $A_{\rm V} = 4$, with a likelihood that decreases up to values of $A_{\rm V} \sim 50$ but then maintains a constant likelihood for higher values of $A_{\rm V}$. The estimated dispersion for this parameter is thus extremely high $\sigma_{A_{\rm V}} \sim 85$ and the χ^2 for the combined model diverges to infinity. Even though there are not many data points constraining the stellar emission in the SED, the best fit model appears to provide a good fit to the data, with a stellar mass of $M_{\rm gal} \simeq 1.3 \times 10^{11}$ M$_\odot$, and thus we do not exclude this object from our analysis.
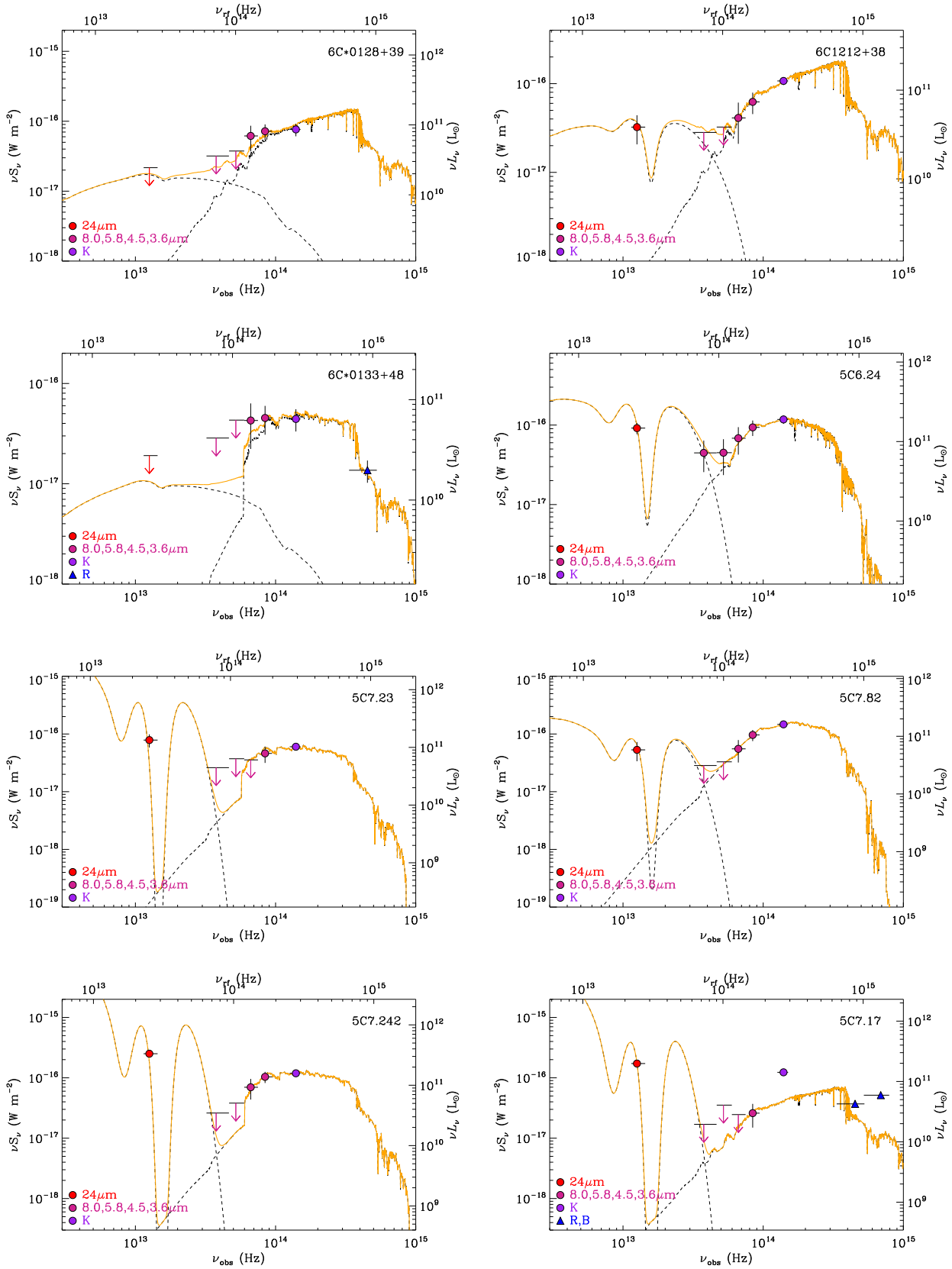
6C1212+38 is not detected at 8.0 and 5.8 μm at a 2σ level. The best fit model is found for a high $A_{\rm V} \sim 39$, with a standard deviation of the same order of magnitude, $\sigma_{A_{\rm V}} \sim 34$, and for a stellar mass of $M_{\rm gal} \simeq 1.6 \times 10^{11}$ M$_\odot$.
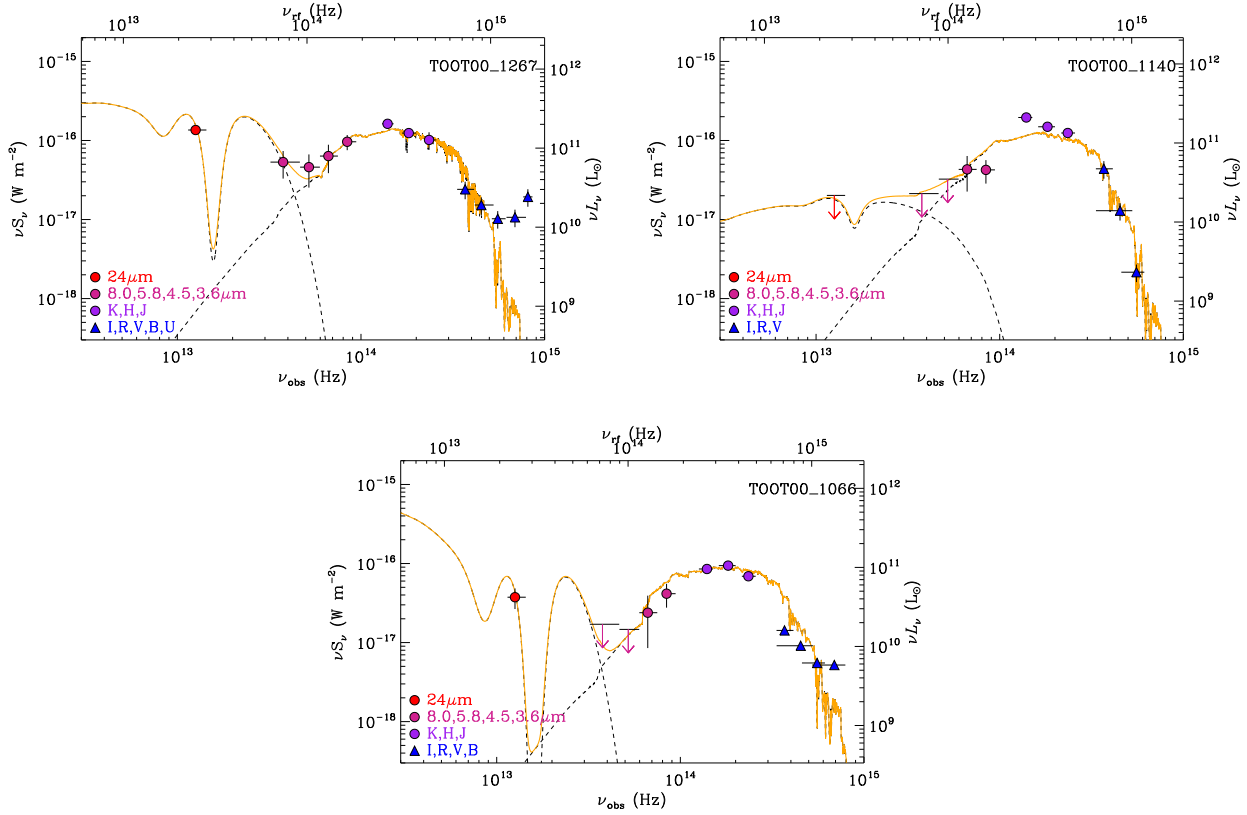
6C*0133+48 is not detected at 24, 8.0 or 5.8 μm at the 2σ
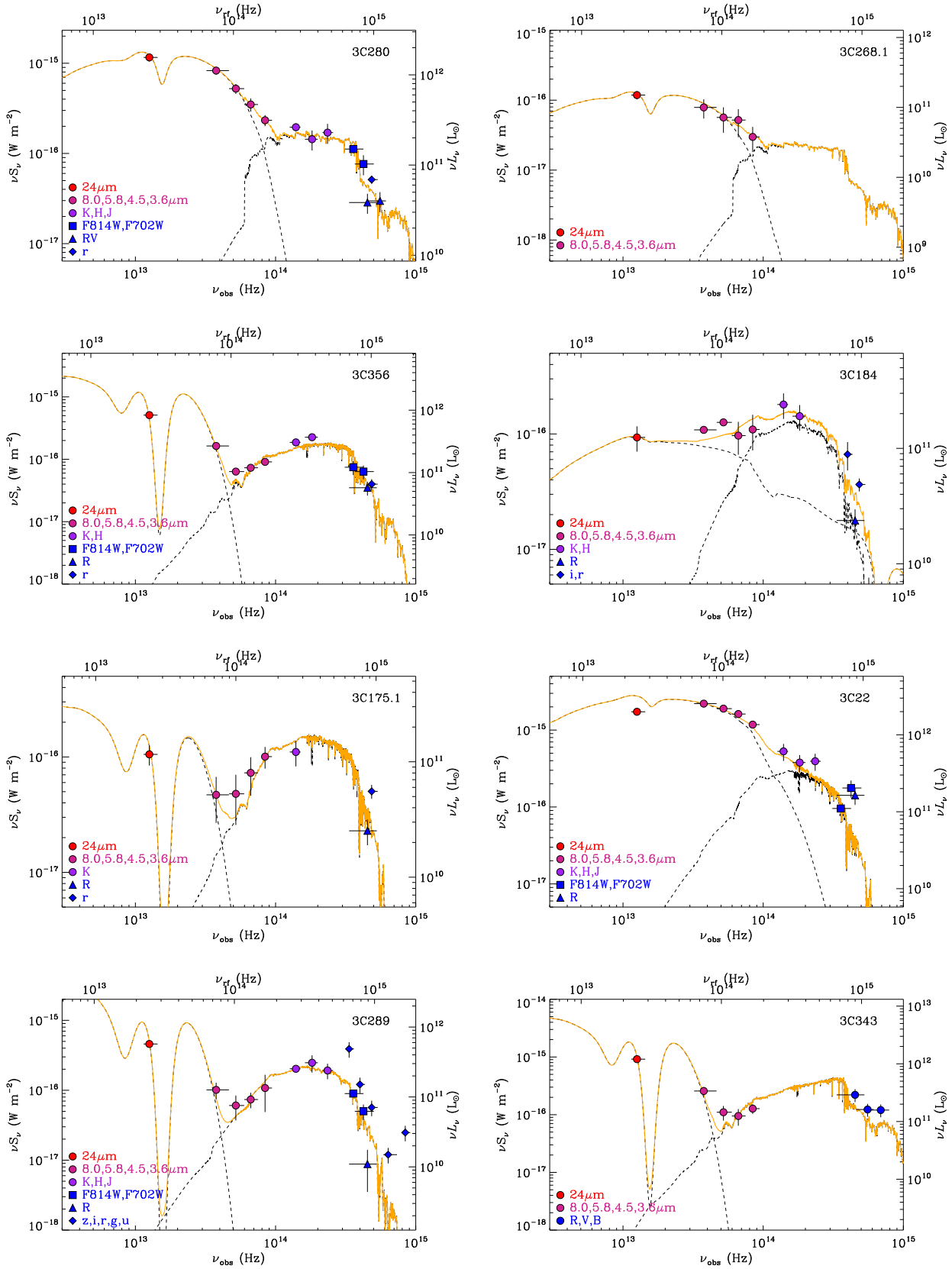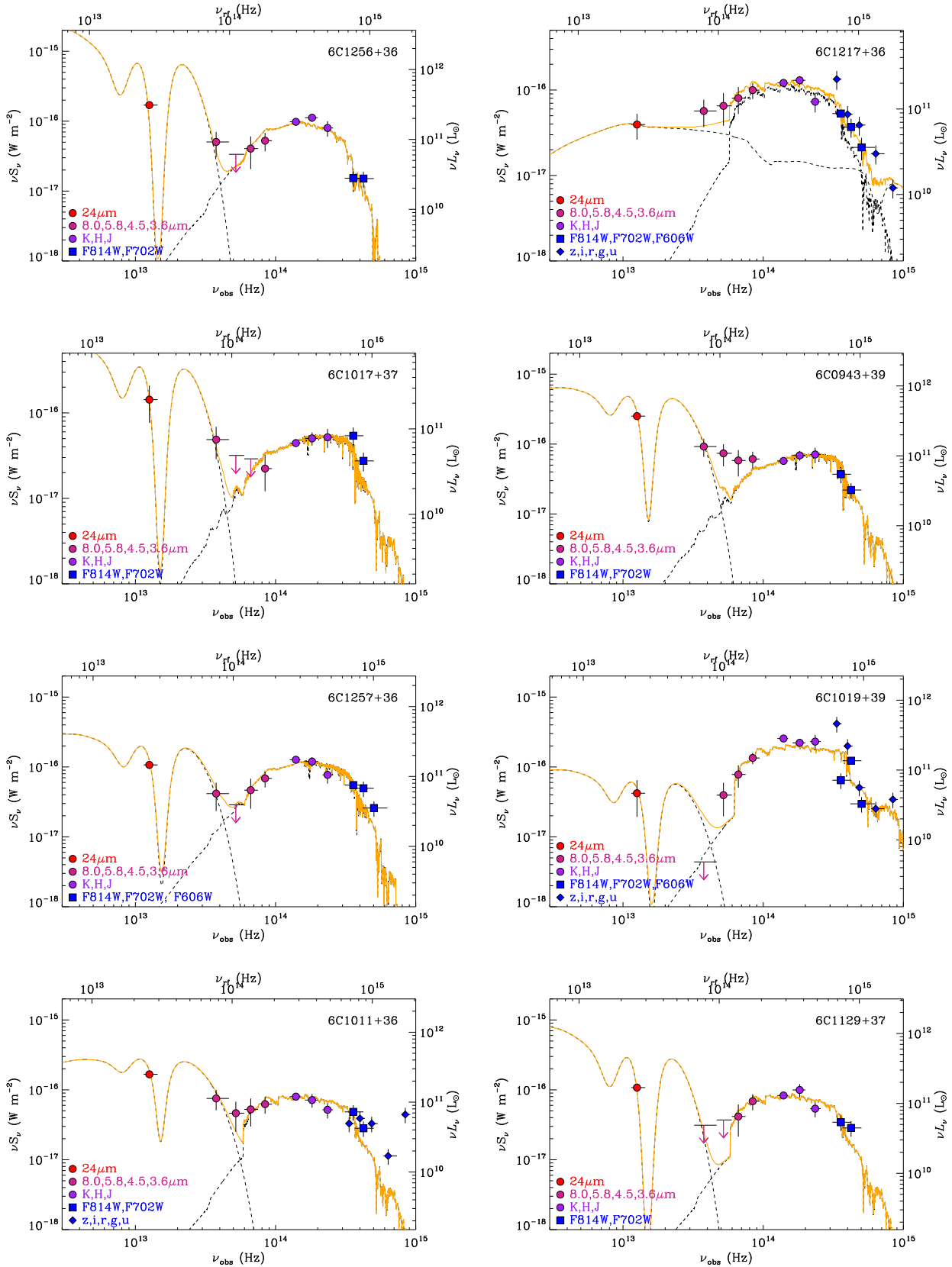
Figure 1. SED fitting of the radio galaxies in our sample. The dashed lines represent both the quasar template affected by dust and the stellar template, whose sum is the model that best fits the data. The solid orange line represents the model that best fits the data. The points represent the data and their error bars. Symbols are as follows: red circles are for $12\mu m$ MIPS data; violet circles are for $8\mu m$, $5.8\mu m$, $4.5\mu m$, and $3.6\mu m$ IRAC data; purple circles are for K, H, and J band data; blue squares are for Hubble F814W, F702W, and F606W band data; blue triangles are for I, R, V, B, and U band data; blue diamonds are for z, i, r, g, and u band data. The undetections are represented as downward arrows.

level, and thus the quasar light component fit is not reliable, with a likelihood very similar to that for 6C*0128+39. The best fit model was found for $A_V = 3.0$ with a much higher standard deviation of $\sigma_{A_V} \sim 42$. However, the stellar dominated part of the SED appears well fitted by a stellar mass of $M_{gal} \simeq 5 \times 10^{10}\,M_\odot$.

5C6.24 has a best fit model with $A_V \sim 84$, and a stellar mass of $M_{gal} \simeq 5.7 \times 10^{11}\,M_\odot$.

5C7.23 is not detected at 8.0, 5.8 and $4.5\,\mu m$ at a 2σ level, and the quasar light component fit does not converge to a specific value of A_V. We determine a lower limit for the visual dust extinction of $A_V > 5$. The stellar mass is constrained mainly with the $3.6\,\mu m$ and K-band data points and a best value of $M_{gal} \simeq 1.1 \times 10^{11}\,M_\odot$ is found.

5C7.82 is not detected at 8.0 and $5.8\,\mu m$ at a 2σ level, and the quasar light component fit has a rather high error associated. The best fit parameter values is $A_V = 146$. The stellar dominated part of the SED looks well constrained by a model with stellar mass $M_{gal} = 6.8 \times 10^{11}\,M_\odot$.

5C7.242 is not detected at 8.0 and $5.8\,\mu m$ at the 2σ level, and thus the quasar light component fit is not entirely reliable. The best fit model was found for an extremely high value of visual extinction, $A_V = 355$, and a stellar mass of $M_{gal} \simeq 1.8 \times 10^{11}\,M_\odot$.

5C7.17 is not detected at 8.0, 5.8 and $4.5\,\mu m$ at the 2σ level, and the quasar light component fit is quite problematic. The best model was found with an extremely high value of visual extinction, $A_V = 353$. The stellar mass value that produces the best model is $M_{gal} \simeq 6 \times 10^{10}\,M_\odot$, with a set of data that is also rather hard to fit, and thus with a large associated error. The high fluxes of the optical data points compared to the stellar population model suggests that these might be contaminated by scattered light as discussed in Section 4 or have ongoing star formation.

TOOT00_1267 has a best fit model with a visual extinction value of $A_V = 103$, and a stellar mass of $M_{gal} \simeq 8.5 \times 10^{11}\,M_\odot$. The high fluxes of the optical data points compared to the galaxy light model suggest that these might be contaminated by scattered light or ongoing star formation.

TOOT00_1140 is not detected at 8.0, 5.8 and $4.5\,\mu m$ at the 2σ level. The best fit model has $A_V \sim 20$. The stellar component is well constrained by a model with a stellar mass of $M_{gal} \simeq 5.9 \times 10^{11}\,M_\odot$.

TOOT00_1066: is not detected at 8.0 and $5.8\,\mu m$ at the 2σ level. The best fit model is found with a high $A_V \sim 232$,

Table 2. Best-fit parameters for our sample of radio galaxies. We note that the fits to 3C268.1 are unreliable due to a lack of data. **Column 1** gives the object name; **Column 2** gives the value of A_V of the best fit model for the SED of the object; **Column 3** gives the 1σ error associated with the A_V value; **Column 4** gives the value of $\log_{10}(M_{gal})$ of the best fit model for the SED of the object; **Column 5** gives the 1σ error associated with the $\log_{10}(M_{gal})$ value; **Column 6** gives the stellar age of the stellar synthesis population model that best fitted the data (BC03 - Bruzual & Charlot 2003; M05 - Maraston 2005) **Column 7** gives the reduced χ^2 of the best-fit model.

Object (1)	A_V (2)	σ_{A_V} (3)	$\log_{10}(M_{gal}/M_\odot)$ (4)	$\sigma_{\log_{10}(M_{gal})}$ (5)	SSP model (6)	χ^2_{red} (7)
3C280	19	2	11.20	0.04	0.5 Gyr (M05)	2.006
3C268.1	17	6	10.33	0.42	0.5 Gyr (M05)	0.190
3C356	127	16	11.60	0.04	1 Gyr (BC03)	3.114
3C184	1.5	0.4	11.82	0.11	5 Gyr (M05)	2.655
3C175.1	123	117	11.58	0.04	2 Gyr (BC03)	3.725
3C22	7	1.3	12	0.04	6 Gyr (BC03)	2.669
3C289	209	48	11.95	0.03	4 Gyr (M05)	4.943
3C343	158	26	11.63	0.05	0.5 Gyr (BC03)	2.683
6C1256+36	180	66	11.89	0.03	6 Gyr (M05)	1.837
6C1217+36	1	0.1	11.30	0.03	1 Gyr (M05)	1.387
6C1017+37	141	63	11.06	0.03	1 Gyr (BC03)	1.227
6C0943+39	99	46	11.16	0.03	1 Gyr (BC03)	1.192
6C1257+36	112	16	11.57	0.03	2 Gyr (BC03)	1.560
6C1019+39	110	125	11.20	0.02	0.5 Gyr (M05)	5.025
6C1011+36	65	37	11.13	0.03	1 Gyr (M05)	3.664
6C1129+37	164	17	11.16	0.03	1 Gyr (M05)	0.858
6C*0128+39	4	85	11.10	0.08	0.5 Gyr (BC03)	Inf.
6C1212+38	39	34	11.20	0.04	0.5 Gyr (BC03)	0.161
6C*0133+48	3	42	10.70	0.08	0.5 Gyr (M05)	0.542
5C6.24	84.0	22	11.76	0.04	3 Gyr (BC03)	0.351
5C7.23	> 5		11	0.05	1 Gyr (M05)	Inf.
5C7.82	146	134	11.83	0.04	5 Gyr (M05)	0.012
5C7.242	355	14	11.26	0.04	1 Gyr (M05)	0.060
5C7.17	353	23	10.78	0.17	0.5 Gyr (BC03)	0.179
TOOT00_1267	103	15	11.93	0.03	6 Gyr (BC03)	4.744
TOOT00_1140	20	5	11.77	0.03	6 Gyr (M05)	8.256
TOOT00_1066	232	46	11.29	0.03	2 Gyr (M05)	0.570

and for a stellar mass of $M_{gal} \simeq 1.9 \times 10^{11}\ M_\odot$.

6 DISCUSSION

The SED fitting provides a good estimation for important physical properties of the radio galaxies such as bolometric luminosity, extinction properties and stellar mass. The stellar mass, in particular, grants, for elliptical galaxies, an accurate estimation of its supermassive black hole mass. Together with the bolometric luminosity, the Eddington weighted accretion rates of the sample can be inferred. In this section, first the extracted physical properties of our sample of radio galaxies are discussed and then the classification of each galaxy into HEG or LEG is used to investigate the HEG/LEG dichotomy at $z \sim 1$.

6.1 Physical properties of the sample

6.1.1 Visual extinction

Our visual extinction estimations are complicated by the fact that at $z \sim 1$, the $24\,\mu m$ data point lies on the edge of

the $10\,\mu m$ silicate feature and thus more data points, or spectroscopic data, would be desirable to better constrain the values of A_V. Nonetheless, previous work in the literature, such as Cleary et al. (2007), agree reasonably well with the values found. In their study of galaxies and quasars from the 3CRR survey at $0.4 \leqslant z \leqslant 1.2$, Cleary et al. (2007) fit IRS and MIPS Spitzer data, and other measurements from the literature, using models with a synchrotron and a dust component. They consider two variations of the dust component, one with a screen of cooler dust, and another with a mixture of warm dust emitting in the MIR and cooler dust. The visual extinction of their sample ranges from $0 < A_V < 40$ for the screen dust component model, and $0 < A_V < 150$ for the mixed dust component model. In particular, for the common objects in our sample and their sample, we find that the values of A_V for 3C268.1, 3C280 and 3C22 agree well with those of Cleary et al. (2007) for a screen dust component. For 3C343 our model is best fit with a dust component with an $A_V = 158$, whereas Cleary et al. (2007) find an $A_V \sim 31$ for a mixed dust component, and $A_V \sim 22$ for a screen dust component, both of them much lower than our value. However, we note that this object does exhibit a steeply rising slope towards mid-infrared wavelengths in the *Spitzer*-IRS data, similar to what we find with our photometry. Our estimated high AGN extinction is inconsistent

with the classification of 3C343 as a quasar by Cleary et al. (2007). However, it is possible that this difference results from an A_V overestimation of our model due to the proximity of the $24\,\mu m$ data point to the $10\,\mu m$ feature.

6.1.2   Stellar mass and Black hole mass

Pioneering studies like those of Kormendy & Richstone (1995), Faber et al. (1997) and Magorrian et al. (1998) established that the hot stellar component of galaxies - i.e. the bulge - is proportional to their black hole mass. This relation became known as the $M_{\rm BH}$-$M_{\rm bulge}$ relation, and Magorrian et al. (1998) found the black hole-to-bulge mass ratio to be approximately 0.006. More recent studies of this relation (e.g. Häring & Rix 2004) find that the median black hole mass is 0.14 per cent of the bulge mass for nearby galaxies, $M_{\rm BH} = 0.0014 M_{\rm bulge}$. We note that including the intrinsic scatter of the $M_{\rm BH} - M_{\rm bulge}$ relation does not make any difference to our results, as the uncertainties in our stellar mass estimates dominate the error budget.

We can use the stellar mass of the galaxy, $M_{\rm gal}$, provided by the SED fitting, along with the $M_{\rm BH}$-$M_{\rm bulge}$ relation to estimate the black hole mass, $M_{\rm BH}$. We assume that there is no significant evolution of the $M_{\rm BH}$-$M_{\rm bulge}$ relation at $z \sim 1$ from the local $M_{\rm BH}/M_{\rm bulge}$. In fact, McLure et al. (2006) shows that for low redshift ($z \lesssim 1$) radio-loud AGN the black hole to spheroid mass ratio lies within the uncertainties of that found in the local Universe. Sarria et al. (2010) also find that obscured AGNs at $z \sim 1 - 2$ are fully consistent with the local $M_{\rm BH}$-$M_{\rm bulge}$ relation. We thus use the local Universe relation $M_{\rm BH} \sim 0.0014 M_{\rm bulge}$. The values found for $M_{\rm gal}$ and $M_{\rm BH}$ are presented in Table 3.

The SED models of the observed photometry bands provide a very good fit for the stellar mass of our objects. In fact, in similar studies to this, Seymour et al. (2007) found that, for a sample of 70 radio galaxies at $1 < z < 5.2$, their broad-band photometry implied stellar masses in the range $10^{11} - 10^{12}\,{\rm M_\odot}$, with a mean mass of $\sim 10^{11.55}\,{\rm M_\odot}$ up to redshifts of $z = 3$. The radio galaxies in our sample have an average stellar mass of $10^{11.59}\,{\rm M_\odot}$ (excluding 3C268.1, for which the stellar mass estimation is poorly constrained), consistent with the study of Seymour et al. (2007).

McLure et al. (2006) estimated the black hole mass of powerful radio quasars from the 3CRR survey with redshifts between $0 < z < 2$ using the virial mass estimator for MgII emission line (McLure & Jarvis 2002; McLure & Dunlop 2004), and estimated black hole masses in the range $10^{8.3}\,{\rm M_\odot} - 10^{10.1}\,{\rm M_\odot}$. The radio galaxies in our sample at $z \sim 1$ have black hole masses in the range $10^{7.8}\,{\rm M_\odot} - 10^{9.4}\,{\rm M_\odot}$ if we exclude 3C268.1. These are consistent with the range of values found in the literature for similar objects. This reinforces the view that powerful radio sources reside in the most massive galaxies with the most massive black holes.

6.1.3   Accretion rate

The bolometric radiative power of an AGN, $L_{\rm bol}$, is proportional to the accretion rate of the black hole, $\dot{M}$, and to the fraction of accreted mass that is radiated, i.e. the radiative

efficiency, ϵ, through the expression:

$$L_{\rm bol} = \epsilon \dot{M} c^2. \qquad (9)$$

Assuming that ϵ takes the fiducial value of 0.1 (e.g. Marconi et al. 2004; Shankar et al. 2004; Martínez-Sansigre & Taylor 2009), we can determine the accretion rate of our sources using their estimated bolometric luminosity, $L_{\rm bol}$. We calculate the values of $L_{\rm bol}$ from the rest-frame $12\mu m$ luminosity, as in Fernandes et al. (2011), using a bolometric correction of 8.5 (e.g. Richards et al. 2006, fig.12), i.e. $L_{\rm bol} = 8.5\lambda L_{12\mu m}$. Our estimated values for the accretion rate are shown in Table 3.

As reviewed by Peterson (1997, sec.3.1), according to the most widely accepted model, radiatively efficient AGNs are powered by gravitational infall of material onto a supermassive black hole, with this material achieving high temperatures in the dissipative accretion disk (e.g. Salpeter 1964). For the material in the galaxy to be in hydrostatic equilibrium, the inward gravitational force needs to be balanced by the outwards radiation pressure. The Eddington luminosity, $L_{\rm Edd}$, is the maximum luminosity that a body needs to be radiating to remain in hydrostatic equilibrium in the case of spherical accretion, assuming a pure ionized hydrogen plasma. This energy is a function of the mass of the system and is given by $L_{\rm Edd} = 1.3 \times 10^{31} \left(\frac{M_{\rm BH}}{M_\odot} \right)$ W. The Eddington ratio, λ is therefore simply,

$$\lambda \equiv \frac{L_{\rm bol}}{L_{\rm Edd}}. \qquad (10)$$

This gives an estimate of the actual accretion rate of the AGN, compared to the maximal Eddington accretion rate.

Having the black hole mass and the accretion rate, we use equations 9 and 10 to estimate the Eddington ratio of the sources in our sample. The values obtained are shown in Table 3. The accretion rate properties of our sample are detailed in the following section.

6.2   The HEG/LEG dichotomy

Table 3 shows how the radio galaxies in our sample are distributed in terms of their optical/near-IR spectral classification. This classification was either taken from the literature, where available (see references in Table 3), or determined by inspecting the optical spectra of the objects. We label the reddened quasar 3C22 (Rawlings et al. 1995; Simpson et al. 1999), and distinguish it as a different class (RQ).

6.2.1   Relation between $L_{\rm 151MHz}$ and λ

First we discuss the relationship between the jet activity and the accretion rate. In Figure 2 we show the distribution of the Eddington ratio versus 151 MHz radio luminosity, where objects of distinct optical classifications are displayed in different colours.

The full sample shows a modest positive correlation between 151 MHz radio luminosity and Eddington ratio. The Spearman coefficient for this correlation is $\rho = 0.42$ and the standard deviation in the Spearman Rank correlation is $\sigma_\rho = 0.03$.

Apart from objects 6C0943+39 and 6C*0128+39, which

Table 3. Column 1 gives the object name; **Column 2** gives the black hole masses; **Column 3** gives the bolometric luminosity; **Column 4** gives the accretion rate; **Column 5** gives the Eddington ratio; **Column 6** gives the optical classification of the object according to the literature. 'HEG' stands for high-excitation radio galaxy, 'LEG' stands for low-excitation radio galaxy, RQ stands for reddened quasar; **Column 7** gives the reference for the optical classification in Column 6 (for the 3CRR, 6CE and 6C* objects) or the reference for the optical spectra (for the 7CRS and TOOT00 objects). References are as follows: Grimes - www-astro.physics.ox.ac.uk/~sr/grimes; J01 - Jarvis et al. 2001b; JR97 - Jackson & Rawlings 1997; REL01 - Rawlings et al. 2001; W03 - Willott et al. 2003; V10 - Vardoulaki et al. 2010

| Object (1)	$\log_{10}(M_{\mathrm{BH}}/\mathrm{M}_\odot)$ (2)	$\log_{10}(L_{\mathrm{bol}}/\mathrm{W})$ (3)	$\log_{10}(\dot{M}/\,\mathrm{M}_\odot/\mathrm{yr})$ (4)	λ (5)	Opt. Class (6)	Ref (7)
3C280	8.346±0.425	39.707±0.012	0.953±0.012	$1.765^{+0.882}_{-0.710}$	HEG	JR97
3C268.1	7.476±4.204	38.689±0.057	-0.065±0.057	$1.257^{+104.822}_{-1.245}$	HEG	JR97
3C356	8.746±0.425	39.435±0.021	0.681±0.021	$0.375^{+0.178}_{-0.155}$	HEG	JR97
3C184	8.966±1.062	38.608±0.110	-0.146±0.110	$0.034^{+0.065}_{-0.024}$	HEG	JR97
3C175.1	8.726±0.425	38.578±0.088	-0.176±0.088	$0.055^{+0.027}_{-0.022}$	HEG	JR97
3C22	9.366±0.425	39.813±0.010	1.059±0.010	$0.215^{+0.103}_{-0.088}$	RQ	JR97
3C289	9.096±0.255	39.271±0.020	0.517±0.020	$0.115^{+0.026}_{-0.034}$	HEG	JR97
3C343	8.776±0.467	39.594±0.014	0.840±0.014	$0.506^{+0.286}_{-0.219}$	HEG	Grimes
6C1256+36	9.036±0.297	39.005±0.040	0.251±0.040	$0.072^{+0.020}_{-0.024}$	HEG?	REL01
6C1217+36	8.446±0.297	38.331±0.151	-0.423±0.151	$0.059^{+0.022}_{-0.020}$	HEG?	REL01
6C1017+37	8.206±0.340	38.855±0.051	0.101±0.051	$0.343^{+0.127}_{-0.118}$	HEG	REL01
6C0943+39	8.306±0.297	39.082±0.033	0.328±0.033	$0.459^{+0.123}_{-0.154}$	LEG?	REL01
6C1257+36	8.718±0.263	38.678±0.056	-0.076±0.056	$0.070^{+0.016}_{-0.021}$	HEG	REL01
6C1019+39	8.346±0.212	38.182±0.263	-0.572±0.263	$0.053^{+0.017}_{-0.019}$	LEG?	REL01
6C1011+36	8.276±0.297	38.911±0.049	0.157±0.049	$0.332^{+0.096}_{-0.108}$	HEG	REL01
6C1129+37	8.306±0.340	38.740±0.061	-0.014±0.061	$0.209^{+0.072}_{-0.074}$	HEG?	REL01
6C*0128+39	8.246±0.849	37.795±0.328	-0.959±0.328	$0.027^{+0.040}_{-0.018}$	HEG?	J01
6C1212+38	8.346±0.425	38.097±0.164	-0.657±0.164	$0.043^{+0.023}_{-0.019}$	LEG	REL01
6C*0133+48	7.846±0.849	37.690±0.702	-1.064±0.702	$0.054^{+0.108}_{-0.038}$	LEG?	J01
5C6.24	8.906±0.425	38.682±0.072	-0.072±0.072	$0.046^{+0.023}_{-0.019}$	HEG	W03
5C7.23	8.196±0.500	38.640±0.115	-0.114±0.115	$0.214^{+0.134}_{-0.098}$	HEG	W03
5C7.82	8.976±0.382	38.278±0.167	-0.476±0.167	$0.015^{+0.007}_{-0.006}$	LEG?	W03
5C7.242	8.406±0.382	39.036±0.035	0.282±0.035	$0.328^{+0.144}_{-0.122}$	HEG?	W03
5C7.17	7.926±1.699	38.811±0.056	0.057±0.056	$0.590^{+2.798}_{-0.503}$	HEG	W03
TOOT00_1267	9.076±0.255	38.743±0.049	-0.011±0.049	$0.036^{+0.007}_{-0.011}$	HEG	V10
TOOT00_1140	8.916±0.255	37.779±0.294	-0.975±0.294	$0.006^{+0.002}_{-0.002}$	LEG	V10
TOOT00_1066	8.436±0.340	38.136±0.130	-0.618±0.130	$0.039^{+0.016}_{-0.014}$	LEG?	V10

have the most uncertain classification into HEG/LEGs, there is a clear trend for the most luminous radio galaxies, with the highest Eddington ratios to be HEGs, or reddened quasars, and, conversely, for LEGs to have lower λ and $L_{151\mathrm{MHz}}$ values. The complete HEG population in our sample have a mean Eddington ratio of $\lambda \approx 0.33$ whereas LEGs have a lower mean of $\lambda \approx 0.09$. Excluding the two outliers that have uncertain classification, 6C0943+39 and 6C*0128+39, though, the mean ratio for HEGs is $\lambda \approx 0.35$ and LEGs is $\lambda \approx 0.03$. We used a Kolmogorov-Smirnov (K-S) test to evaluate whether the HEGs have a statistically different distribution in their accretion rate compared to LEGs, and found, for the full sample, $D = 0.66$ with an associated probability of $p = 0.01$, rejecting the null hypothesis that the two populations are drawn from the same underlying distribution at a 99 per cent level. A Mann-Whitney test also yields a 97 per cent probability that the null hypothesis that the two populations HEGs and LEGs come from the same distribution is not supported by the data. The transition from LEG to HEG appears to occur around $\lambda \sim 0.04$, which is in excellent agreement with the theoretical expecta-tions of where accretion rate becomes radiatively inefficient (e.g. Rees et al. 1982; Narayan & Yi 1995; Esin et al. 1997).

The distribution of HEGs and LEGs with respect to radio luminosity seems indistinguishable up to 151 MHz luminosities of $\sim 3 \times 10^{27}\,\mathrm{W\,Hz^{-1}\,sr^{-1}}$. For higher luminosities HEGs fully dominate the sample. Even though the literature generally states a bias for FRI radio galaxies to be predominantly LEGs, and FRIIs a mix of both HEGs and LEGs (e.g. Hine & Longair 1979; Laing et al. 1994), there have been recent studies showing that HEGs and LEGs span a similar range of radio luminosities (e.g. Best & Heckman 2012) in the local Universe. If the radio properties of HEGs and LEGs are indeed indistinguishable, and the HEG and LEG distinction is due to the accretion process, this means that the mechanism that generates the jets in both HEGs and LEGs is not solely related to the accretion rate, and other physical processes must also play an important role, such as black hole spin.
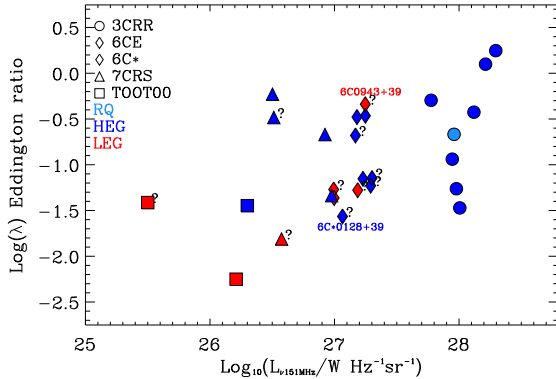
Figure 2. Relation between low frequency radio luminosity and Eddington ratio. Symbols are: circles for the 3CRR survey objects, diamonds for the 6CE and the 6C* surveys, triangles for the 7CRS, and squares for the TOOT00 survey objects. Objects coloured in red are classified as LEGs, objects in dark blue are HEGs, and those in light blue are reddened quasars. '?' denotes objects whose classification is uncertain. The two outliers to the general trend are identified with their names. Both of them have an uncertain classification.
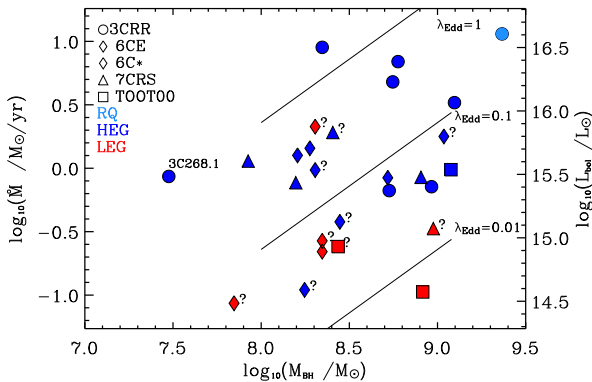
Figure 3. Black hole mass and accretion rate distribution for HEGs and LEGs. Symbols are as in Figure 2. The right axis shows $L_{\rm bol}$ estimated from $\dot{M}$ using equation (9). Object 3C268.1 is identified as it has an unreliable mass estimation (see Section 5).

6.2.2 Relation between $M_{\rm BH}$ and $\dot{M}$

From equations (9) and (10), the black hole mass and accretion rate can be related through:

$$\dot{M} = \frac{\lambda}{\epsilon c^2} 1.3 \times 10^{31} \left(\frac{M_{\rm BH}}{M_\odot} \right) \text{ W.} \qquad (11)$$

If we assume the radiative efficiency to be constant, then the slope of the relationship between black hole mass and accretion rate should provide information on the Eddington ratio. The Eddington ratio is thus proportional to the radiative efficiency times $\dot{M}/M_{\rm BH}$. The distribution of the inferred accretion rate and bolometric luminosity versus black hole mass is shown in Figure 3.

We observe a general trend for more massive black holes to have higher accretion rates. The sources in our sample of
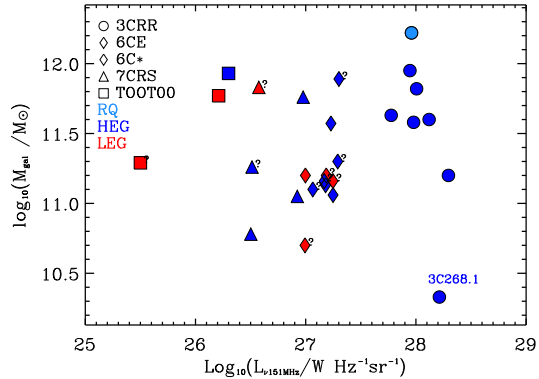
Figure 4. Distribution of stellar mass for the two populations HEGs and LEGs. Symbols are as in Figure 2. Object 3C268.1 is identified as it has an unreliable mass estimation (see Section 5).

galaxies have Eddington ratios of $0.005 < \lambda < 1.7$ with only 3C280 measured to be accreting above Eddington, albeit with a large uncertainty.

The distribution seen in Eddington ratios could either be due to the accretion rate, or to the black hole mass. Figure 3 shows that accretion onto the black hole is the dominant factor for the separation between the two classes, given the large overlap in black hole mass. Therefore, acknowledging HEGs and LEGs as being powered by different modes of accretion - i.e. radiatively efficient and radiatively inefficient, respectively - the rate at which matter is being accreted onto the supermassive black hole is determinant for the accretion mode. Furthermore, the HEGs in our sample have similar accretion rates to quasars at $z \sim 1$ selected from the SDSS survey which have $\log_{10}(\lambda) \sim -0.5$ (McLure & Dunlop 2004), compared to a mean of $\log_{10}(\lambda) = -0.47^{+0.009}_{-0.03}$ for the HEG radio galaxies in our sample. This is consistent with unified models in which radio-loud quasars and HEGs are similar objects viewed at different orientations (e.g. Barthel 1989).

6.2.3 Host galaxies of HEGs and LEGs

For a large sample of radio galaxies in the local Universe, Best & Heckman (2012) find evidence that HEGs are hosted by less massive galaxies relative to LEGs. At $z \sim 1$, we do not observe any clear difference between the host galaxy masses of HEGs and LEGs in our much smaller sample (see Figure 4). Given that our sample was selected to include the most powerful radio sources, we can expect it to be biased towards the largest masses.

McLure et al. (2004) and Herbert et al. (2011) have found that for a similar sample of radio galaxies at $z \sim 0.5$, HEGs demonstrate a significant correlation between $M_{\rm BH}$ and $L_{\rm 151MHz}$. McLure et al. (2004) also note that the TOOT objects deviate from the $M_{\rm BH}$ and $L_{\rm 151MHz}$ correlation, and have higher mean galaxy masses than other subsamples, such as 7CRS and 6CE, which probe higher radio luminosities. With a larger redshift span, however, Seymour et al. (2007) find only a weak correlation between stellar mass and radio luminosity.

In our sample we do not find a strong correlation between $M_{\rm gal}$ and $L_{\rm 151MHz}$ for the full sample of HEGs. Even
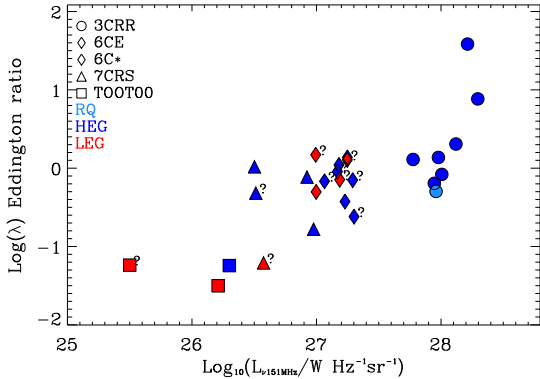
Figure 5. Relation between low frequency radio luminosity and Eddington ratio, including the jet power contribution in the Eddington ratio calculation as detailed in the text. Symbols are as in Figure 2.

Figure 6. Black hole mass and accretion rate distribution for HEGs and LEGs, including the jet power contribution in the accretion rate calculation. Symbols are as in Figure 2. The right axis shows $L_{\rm bol}$ estimated from $\dot{M}$ using equation (9).

dismissing 3C268.1, which has an unreliable mass estimation (see Section 5), the correlation between $M_{\rm gal}$ and $L_{\rm 151MHz}$ has a Spearman rank correlation coefficient of $\rho = 0.39$ and a standard deviation of $\sigma_\rho = 0.09$, not highly significant.

### 6.2.4 Accounting for the jet power in the accretion rate

Most studies in the literature define the Eddington ratio as in section 6.1.3, however some studies consider a more physical approach is to include the contribution of the jet mechanical energy in the output of the accretion energy, i.e. the total energy produced due to the accretion process should equal the sum of the radiative luminosity and the jet mechanical luminosity (e.g. Hardcastle et al. 2007; Best & Heckman 2012; Mingo et al. 2014). Considering the Eddington luminosity as a normalisation factor to compare systems over a wide range of luminosities, the total Eddington ratio is in fact an Eddington-scaled accretion rate. The radiative output alone does not account for the total Eddington accretion, hence neglecting the contribution of the jet kinetic energy would underestimate the energy output from the accretion process. This may be particularly important in LEGs, for which the radiative energy is much lower and the jet power is an important component of the total energy budget.

Figure 5 shows the Eddington ratio distribution with radio 151 MHz luminosity, as in Figure 2, but including the contribution of $Q_{\rm jet}$, i.e.:

$$\lambda_{\rm rad+mec} \equiv \frac{L_{\rm bol} + Q_{\rm jet}}{L_{\rm Edd}}, \qquad (12)$$

where $\lambda_{\rm rad+mec}$ is the Eddington ratio accounting for both the radiative energy and the jet mechanical energy. We estimate the jet power using the relation $Q_{\rm jet} \simeq 3 \times 10^{38} f^{3/2} (L_{\nu 151MHz}/10^{28})^{6/7} {\rm W}$ (Willott et al. 1999), where $1 \leqslant f \leqslant 20$ represents several uncertainties associated with estimating $Q_{\rm jet}$ from $L_{\nu 151MHz}$. Following Fernandes et al (2011), we chose $f = 10$ as this is the expectation value of a flat prior in natural space.

The Spearman rank test, with a Spearman coefficient of $\rho \sim 0.59$ and $\sigma_\rho = 0.001$, reflects a tighter correlation between 151 MHz radio luminosity and Eddington ratio with
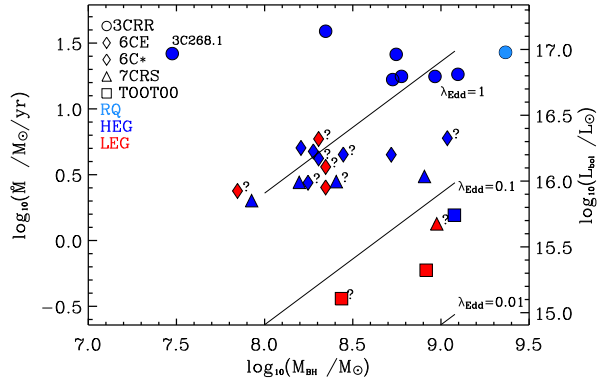
the inclusion of $Q_{\rm jet}$ than when accounting solely for the $L_{\rm bol}$.

The separation between HEGs and LEGs is not as clear as when we consider the Eddington scaled accretion rate to be solely dictated by the radiated luminosity $L_{\rm bol}$. Indeed, the K-S test now shows a much lower 64% probability that the two populations come from distinct distributions ($p = 0.36$ and $D = 0.38$). Given that our sample contains the strongest radio galaxies at $z \sim 1$, the jet power is not negligible when compared to the radiative energy.

Figure 6 shows the distribution of accretion rate with black hole mass, where the contribution of the jet mechanical energy is taken into account in the calculation of the accretion rate. The separation between HEGs and LEGs is not as clear as when considering only the radiated energy for the calculation of the accretion rate, however, it is still clear that HEGs have on average higher accretion rates than LEGs. The inclusion of the contribution of $Q_{\rm jet}$ has given rise to a transition range between $0.1 \lesssim \log_{10}(\dot{M}/M_\odot yr^{-1}) \lesssim 0.8$, with both HEGs and LEGs found at these accretion rates. Only LEGs are found at lower accretion rates $\log_{10}(\dot{M}/M_\odot yr^{-1}) < 0.1$, and only HEGs above $\log_{10}(\dot{M}/M_\odot yr^{-1}) > 0.8$.

As expected, an Eddington ratio that only takes into account the radiated luminosity to balance the gravitational pull shows a more clear separation between HEGs and LEGs. Due to the fact that the sources in our sample span a wide range in radio luminosities, and include some of the strongest radio sources at $z \sim 1$, it is expected for the jet mechanical energy of these sources to significantly contribute to the energy balance. This is particularly true for LEGs, where the radiated emission is weaker.

Figure 7 shows the Eddington ratio distribution of HEGs and LEGs obtained with both methods of calculating the Eddington ratio. Solid lines are for $\lambda = (L_{\rm bol} + Q_{\rm jet})/L_{\rm Edd}$ and dashed lines for $\lambda = L_{\rm bol}/L_{\rm Edd}$. The total accretion energy for both HEGs and LEGs is significantly increased, however, the trend for HEGs to show higher Eddington ratios than LEGs remains.
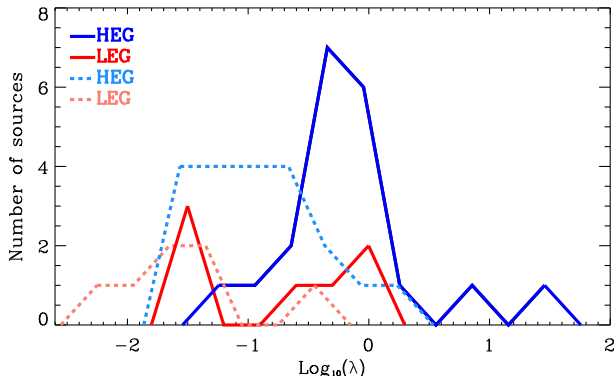
Figure 7. Eddington ratio distribution of HEGs and LEGs. Solid lines are for the Eddington ratio estimated using $\lambda = (L_{\rm bol} + Q_{\rm jet})/L_{\rm Edd}$; dashed lines are for the Eddington ratio estimated using $\lambda = L_{\rm bol}/L_{\rm Edd}$.

7   CONCLUSIONS

We have used *Spitze*r 24μm MIPS and 3.6, 4.5, 5.8, and 8μm IRAC data, as well as near-IR and optical data from the literature, to constrain the SEDs of the sample of radio galaxies previously studied by Fernandes et al. (2011). We applied a dust extinction law to a quasar template to approximate the mid-IR region of the SED, and a template of an elliptical galaxy.

From these fits we are able to determine the black-hole masses through $M_{\rm bulge} - M_{\rm BH}$ relation, the quasar bolometric luminosity, the accretion rate and the Eddington ratio. Our analysis revealed the following:

(i) We find a significant correlation between the Eddington ratio and the radio luminosity, with more luminous radio sources yielding higher Eddington ratios, and thus higher accretion rates.

(ii) We find that HEGs tend to have higher Eddington ratios and radio luminosities, whereas the LEGs in our sample predominantly gather towards the lowest values of λ and $L_{\rm 151MHz}$. We find the HEG/LEG division to lie approximately at $\lambda \sim 0.04$, which is in excellent agreement with theoretical predictions of where the accretion rate becomes radiatively inefficient and also with other studies (Best & Heckman 2012; Mingo et al. 2014). This result further confirms the suspicion that the differences between HEGs and LEGs arise due to the different modes of accretion, which result in different accretion rates. Higher accretion rates are observed with the radiatively efficient 'cold mode' accretion, whereas lower accretion rates can be explained with the radiatively inefficient 'hot mode' of accretion, such as ADAFs.

(iii) By including the contribution of the jet power to the Eddington ratio instead of solely accounting for the radiated power, the HEG/LEG dichotomy becomes less clear. Indeed, the contribution of the jet power is expected to have a significant weight for LEGs, which have a weaker radiated power. Moreover, given that our sample consists of some of the most powerful radio sources, the jet power contribution appreciably increases the Eddington ratios of HEGs as well. The

trend for HEGs to have higher accretion rates than LEGs remains.

(iv) We find that the more massive black holes have higher accretion rates for the HEGs population. HEGs and LEGs are similarly distributed in terms of black hole mass. This relation further displays the dichotomy between HEGs and LEGs in accretion rate, meaning that the dichotomy seen in Eddington ratio is due to the accretion rate and not a dichotomy in black hole mass.

(v) We do not find a strong correlation between the host galaxy mass, or equivalently the black hole mass, and the radio luminosity of the sample. Similarly to Seymour et al. (2007), there is only a slight trend for the highest mass galaxies to host the most powerful radio sources.

(vi) Recent studies in the local Universe find evidence that LEGs are hosted by more massive galaxies than HEGs. However, at $z \sim 1$ we do not observe any difference in terms of host galaxy mass distribution for HEGs and LEGs, although we note that our sample is much smaller than those used in the local Universe.

(vii) It is important to ascertain whether the radio properties of HEGs and LEGs are indistinguishable or not. Our study hints that, at least up to radio luminosities of $\sim 3 \times 10^{27}$ W Hz^{-1} sr^{-1}, HEGs and LEGs span the same range of radio luminosities. If HEGs and LEGs' radio properties are indeed indistinguishable, and the HEG and LEG distinction is due to the accretion process, this means that the power being channeled into the jets is most likely not solely dependent on the accretion rate and an additional process must be influencing the jet formation. Understanding the HEG/LEG dichotomy may thus bring important new constraints on the relation between accretion process and jet formation.

REFERENCES

Antonucci, R. 1993, ARA&A, 31, 473

Barthel, P. D. 1989, ApJ, 336, 606

Begelman, M., & Rees, M. 1996, Scientific American Library, New York: W.H. Freeman, —c1996,

Best, P. N., Longair, M. S., & Roettgering, J. H. A. 1997, MNRAS, 292, 758

Best, P. N., Röttgering, H. J. A., & Longair, M. S. 2000, MNRAS, 311, 1

Best, P. N., & Heckman, T. M. 2012, MNRAS, 421, 1569

Bîrzan, L., Rafferty, D. A., McNamara, B. R., Wise, M. W., & Nulsen, P. E. J. 2004, ApJ, 607, 800

Bower, R. G., Lucey, J. R., & Ellis, R. S. 1992, MNRAS, 254, 601

Bower, R. G., Kodama, T., & Terlevich, A. 1998, MNRAS, 299, 1193

Bruzual, G., & Charlot, S. 2003, MNRAS, 344, 1000

Bryant, J. J., Broderick, J. W., Johnston, H. M., et al. 2009, MNRAS, 394, 2197

Buttiglione, S., Capetti, A., Celotti, A., et al. 2010, A&A, 509, A6

Carollo, C. M., & Danziger, I. J. 1994, MNRAS, 270, 523

Cleary, K., Lawrence, C. R., Marshall, J. A., Hao, L., & Meier, D. 2007, ApJ, 660, 117

Croton D., et al. 2006, MNRAS, 365, 11

Davies, R. L., Sadler, E. M., & Peletier, R. F. 1993, MNRAS, 262, 650

Dunlop, J. S., & Peacock, J. A. 1993, MNRAS, 263, 936

Dunlop, J. S., McLure, R. J., Kukula, M. J., et al. 2003, MNRAS, 340, 1095

Eales, S. A., & Rawlings, S. 1990, MNRAS, 243, 1P

Eales, S., Rawlings, S., Law-Green, D., Cotter, G., & Lacy, M. 1997, MNRAS, 291, 593

Elvis, M., Wilkes, B. J., McDowell, J. C., et al. 1994, ApJS, 95, 1

Esin, A. A., McClintock, J. E., & Narayan, R. 1997, ApJ, 489, 865

Faber, S. M., Tremaine, S., Ajhar, E. A., et al. 1997, AJ, 114, 1771

Fabian, A. C., Celotti, A., Blundell, K. M., Kassim, N. E., & Perley, R. A. 2002, MNRAS, 331, 369

Falder, J. T., et al. 2010, MNRAS, 405, 347

Fernandes, C. A. C., Jarvis, M. J., Rawlings, S., et al. 2011, MNRAS, 411, 1909

Ferrarese, L., & Merritt, D. 2000, ApJL, 539, L9

Floyd, D. J. E., Axon, D., Baum, S., et al. 2010, ApJ, 713, 66

Gebhardt, K., Bender, R., Bower, G., et al. 2000, ApJL, 539, L13

Haas, M., Willner, S. P., Heymann, F., et al. 2008, ApJ, 688, 122

Hardcastle, M. J. 2004, A&A, 414, 927

Hardcastle, M. J., Evans, D. A., & Croston, J. H. 2007, MNRAS, 376, 1849

Häring, N., & Rix, H.-W. 2004, ApJL, 604, L89

Herbert, P. D., Jarvis, M. J., Willott, C. J., et al. 2010, MNRAS, 406, 1841

Herbert, P. D., Jarvis, M. J., Willott, C. J., et al. 2011, MNRAS, 410, 1360

Hernquist, L., & Mihos, J. C. 1995, ApJ, 448, 41

Hill, G. J., & Lilly, S. J. 1991, ApJ, 367, 1

Hill G. J., Rawlings S., 2003, NewAR, 47, 373

Hine, R. G., & Longair, M. S. 1979, MNRAS, 188, 111

Hopkins, P. F., Strauss, M. A., Hall, P. B., et al. 2004, AJ, 128, 1112

Inskip, K. J., Best, P. N., Longair, M. S., et al. 2003, MNRAS, 345, 1365

Inskip, K. J., Best, P. N., & Longair, M. S. 2006, MNRAS, 367, 693

Jackson, N., & Rawlings, S. 1997, MNRAS, 286, 241

Jarvis, M. J., et al. 2001, MNRAS, 326, 1563

Jarvis, M. J., Rawlings, S., Eales, S., Blundell K.M., Bunker A.J., Croft S., McLure R.J., Willott C.J., 2001, MNRAS, 326, 1585

Jarvis, M. J., Bonfield, D. G., Bruce, V. A., et al. 2013, MNRAS, 428, 1281

Kauffmann, G., & Haehnelt, M. 2000, MNRAS, 311, 576

Kauffmann, G., Heckman, T. M., & Best, P. N. 2008, MNRAS, 384, 953

Kormendy, J., & Richstone, D. 1995, ARA&A, 33, 581

Lacy, M., Rawlings, S., Hill, G. J., Bunker A.J., Ridgway S.E., Stern D, 1999, MNRAS, 308, 1096

Laing, R. A., Riley, J. M., & Longair, M. S. 1983, MNRAS, 204, 151

Laing, R. A., Jenkins, C. R., Wall, J. V., & Unger, S. W. 1994, The Physics of Active Galaxies, 54, 201

Lebofsky, M. J. 1981, ApJL, 245, L59

Lilly, S. J., & Longair, M. S. 1984, MNRAS, 211, 833

Magorrian, J., Tremaine, S., Richstone, D., et al. 1998, AJ, 115, 2285

Maraston, C. 2005, MNRAS, 362, 799

Maraston, C., Nieves Colmenárez, L., Bender, R., & Thomas, D. 2009, A&A, 493, 425

Marconi, A., Risaliti, G., Gilli, R., et al. 2004, MNRAS, 351, 169

Martínez-Sansigre, A., Rawlings, S., Bonfield, D. G., et al. 2007, MNRAS, 379, L6

Martínez-Sansigre, A., Karim, A., Schinnerer, E., et al. 2009, ApJ, 706, 184

Martínez-Sansigre, A., & Taylor, A. M. 2009, ApJ, 692, 964

Martínez-Sansigre, A., & Rawlings, S. 2011, MNRAS, 414, 1937

Martinez-Sansigre, A., & Rawlings, S. 2012, arXiv:1201.6591

Mason, R. E., Ramos Almeida, C., Levenson, N. A., Nemmen, R., & Alonso-Herrero, A. 2013, ApJ, 777, 164

Matsumoto, R., & Tajima, T. 1995, ApJ, 445, 767

Medvedev, M. V. 2000, ApJ, 541, 811

McCarthy, P. J. 1993, ARA&A, 31, 639

McLure, R. J., & Jarvis, M. J. 2002, MNRAS, 337, 109

McLure, R. J., & Dunlop, J. S. 2004, MNRAS, 352, 1390

McLure, R. J., Willott, C. J., Jarvis, M. J., et al. 2004, MNRAS, 351, 347

McLure, R. J., Jarvis, M. J., Targett, T. A., Dunlop, J. S., & Best, P. N. 2006, MNRAS, 368, 1395

Mingo, B., Hardcastle, M. J., Croston, J. H., et al. 2014, MNRAS, 440, 269

Narayan, R., & Yi, I. 1995, ApJ, 452, 710

Nenkova, M., Sirocky, M. M., Ivezić, Ž., & Elitzur, M. 2008, ApJ, 685, 147

Padovani, P. 1989, A&A, 209, 27

Peacock, J. A. 1999, Cosmological Physics, by John A. Pea-

cock, pp. 704. ISBN 052141072X. Cambridge, UK: Cambridge University Press, January 1999.,

Pei, Y. C. 1992, ApJ, 395, 130

Peterson, B. M. 1997, An introduction to active galactic nuclei, Publisher: Cambridge, New York Cambridge University Press, 1997 Physical description xvi, 238 p. ISBN 0521473489,

Quataert, E., Dorland, W., & Hammett, G. W. 2002, ApJ, 577, 524

Quataert, E., & Gruzinov, A. 1999, ApJ, 520, 248

Rawlings, S., Lacy, M., Sivia, D. S., & Eales, S. A. 1995, MNRAS, 274, 428

Rawlings, S., Eales, S., & Lacy, M. 2001, MNRAS, 322, 523

Rees, M. J., Begelman, M. C., Blandford, R. D., & Phinney, E. S. 1982, Nature, 295, 17

Renzini, A. 2006, ARA&A, 44, 141

Richards, G. T., Lacy, M., Storrie-Lombardi, L. J., et al. 2006, ApJS, 166, 470

Richstone, D., Ajhar, E. A., Bender, R., et al. 1998, Nature, 395, A14

Rigler, M. A., Stockton, A., Lilly, S. J., Hammer, F., & Le Fevre, O. 1992, ApJ, 385, 61

Roberts, G. O., & Rosenthal, J. S. 1998, Canadian J. Stat. 26, 531.

Salpeter, E. E. 1964, ApJ, 140, 796

Sarria, J. E., Maiolino, R., La Franca, F., et al. 2010, A&A, 522, L3

Schlegel, D. J., Finkbeiner, D. P., & Davis, M. 1998, ApJ, 500, 525

Seymour, N., Stern, D., De Breuck, C., et al. 2007, ApJS, 171, 353

Shakura, N. I., & Sunyaev, R. A. 1973, A&A, 24, 337

Shankar, F., Salucci, P., Granato, G. L., De Zotti, G., & Danese, L. 2004, MNRAS, 354, 1020

Shlosman, I., Begelman, M. C., & Frank, J. 1990, Nature, 345, 679

Shlosman, I., Frank, J., & Begelman, M. C. 1989, Nature, 338, 45

Sikora, M., Stawarz, Ł., & Lasota, J.-P. 2007, ApJ, 658, 815

Silverman, J. D., Lamareille, F., Maier, C., et al. 2009, ApJ, 696, 396

Simpson, C., Rawlings, S., & Lacy, M. 1999, MNRAS, 306, 828

Spolaor, M., Proctor, R. N., Forbes, D. A., & Couch, W. J. 2009, ApJL, 691, L138

Stone, J. M., Hawley, J. F., Gammie, C. F., & Balbus, S. A. 1996, ApJ, 463, 656

Tasse, C., Best, P. N., Röttgering, H., & Le Borgne, D. 2008, A&A, 490, 893

Urry, C. M., & Padovani, P. 1995, PASP, 107, 803

Vardoulaki, E., Rawlings, S., Hill, G. J., et al. 2010, MNRAS, 401, 1709

Willott, C. J., Rawlings, S., Blundell, K. M., & Lacy, M. 1998, MNRAS, 300, 625

Willott, C. J., Rawlings, S., Blundell, K. M., & Lacy, M. 1999, MNRAS, 309, 1017

Willott, C. J. 2001, EAS Publications Series, 1, 109

Willott, C. J., Rawlings, S., Jarvis, M. J., & Blundell, K. M. 2003, MNRAS, 339, 173

Willott, C. J. 2005, ApJL, 627, L101

Wilson, A. S., & Colbert, E. J. M. 1995, ApJ, 438, 62

Wold, M., Lacy, M., Lilje, P. B., & Serjeant, S. 2001, MNRAS, 323, 231

Table 1. J, H, and K band magnitudes found in the literature. "aper. corr", "line cont.", and "Gal. ext." stand for the magnitude values after being corrected for aperture, emission-line contamination, and Galactic extinction, respectively. An error of 25% was assumed for each magnitude value subjected to any of these corrections. The references to the literature magnitudes are: B97 - Best et al. 1997; DP93 - Dunlop & Peacock 1993; E97 - Eales et al. 1997; I03 - Inskip et al. 2003; I06 - Inskip et al. 2006; J01 - Jarvis et al. 2001b; L84 - Lilly & Longair 1984; Leb81 - Lebofsky 1981; LRL83 - Laing et al. 1983; W98 - Willott et al. 1998; W03 - Willott et al. 2003; V10 - Vardoulaki et al. 2010

Object	correction	J	Ref	H	Ref	K	Ref
3C280	literature	18.07 ± 0.05	B97	18.10 ± 0.15 (4)	I06	16.70 ± 0.04	B97
	aper. corr.			17.84			
	line conta.	18.36					
3C356	literature	-	-	17.35 ± 0.13	L84	16.75 ± 0.13	L84
3C184	literature	-	-	17.87 ± 0.12	Leb81	16.80 ± 0.10	Leb81
	Gal. ext.			17.85		16.79	
3C175.1	literature	-	-	-	-	17.56 ± 0.30 (5)	DP93
	aper. corr.					17.35	
	Gal. ext.					17.32	
3C22	literature	17.53 ± 0.08 (4)	I06	16.95 ± 0.09 (4)	I06	15.66 ± 0.05 (4)	I06
	aper. corr.	17.32		16.79		15.62	
	line corr.	17.45					
3C289	literature	18.19 ± 0.06	B97	17.25 ± 0.33	L84	16.66 ± 0.07	B97
	line cont.	18.23					
6CE1256+3648	literature	19.11 ± 0.16	I03	18.11 ± 0.14	I03	17.45 ± 0.07	I03
	line cont.	19.18					
6CE1217+3645	literature	19.26 ± 0.16	I03	17.95 ± 0.13	I03	17.22 ± 0.08	I03
	line cont.	19.28					
6CE1017+3712	literature	19.35 ± 0.2	I03	18.98 ± 0.19	I03	18.31 ± 0.08	I03
	line cont.	19.65					
6CE0943+3958	literature	19.14 ± 0.12	I03	18.64 ± 0.17	I03	18.03 ± 0.11	I03
	line cont.	19.31					
6CE1257+3633	literature	19.15 ± 0.17	I03	18.04 ± 0.17	I03	17.17 ± 0.05	I03
	line cont.	19.22 ± 1.92					
6CE1019+3924	literature	18.00 ± 0.06	I03	17.37 ± 0.09	I03	16.41 ± 0.04	I03
	line cont.	18.03					
6CE1011+3632	literature	19.59 ± 0.28	I03	18.6 ± 0.24	I03	17.67 ± 0.09	I03
	line cont.	19.65					
6CE1129+3710	literature	19.38 ± 0.2	I03	18.24 ± 0.23	I03	17.63 ± 0.11	I03
	line cont.	19.61					
6C*0128+394	literature	-	-	-	-	17.72 ± 0.22	J01
6CE1212+3805	literature	-	-	-	-	17.35 ± 0.08	E97
6C*0133+486	literature	-	-	-	-	18.69 ± 0.27 (5)	J01
	aper. corr.					18.51	
5C6.24	literature	-	-	-	-	17.25 ± 0.13	W03
5C7.23	literature	-	-	-	-	17.98 ± 0.09	W03
5C7.82	literature	-	-	-	-	17.01 ± 0.09	W03
5C7.242	literature	-	-	-	-	17.24 ± 0.09	W03
5C7.17	literature	-	-	-	-	17.37 ± 0.07 (5)	W98
	aper. corr.					17.20	
TOOT1267	literature	18.90 ± 0.13	V10	18.00 ± 0.10	V10	16.90 ± 0.05	V10
	line cont.	18.92					
TOOT1140	literature	18.70 ± 0.12	V10	17.8 ± 0.09	V10	16.7 ± 0.04	V10
	line cont.	18.70					
TOOT1066	literature	19.30 ± 0.15	V10	18.30 ± 0.09	V10	17.60 ± 0.07	V10
	line cont.	19.34					

Table 2. HST F606W, F702W and F814W-band magnitudes found in the literature. "aper. corr" and "line cont." stand for the magnitude values after being corrected for aperture, and emission-line contamination, respectively. An error of 25% was assumed for each magnitude value subjected to any of these corrections. The references to the literature magnitudes are: B97 - Best et al. 1997; I03 - Inskip et al. 2003; I06 - Inskip et al. 2006

Object	correction	F606W	Ref	F702W	Ref	F814W	Ref
3C280	literature	-	-	20.92 ± 0.06 (4)	I06	19.78 ±0.04	B97
	aper. corr.			20.41			
	line conta.			20.53			
3C356	literature	-	-	21.22±0.09	I06	20.60±0.03	I06
	aper. corr.			20.68		20.22	
	line cont.			20.73			
3C22	literature	-	-	20.00 ± 0.15 (4)	I06	19.95±0.03	B97
	aper. corr.			19.57			
	line cont.			19.62			
3C289	literature	-	-	21.49 ± 0.07 (4)	I06	20.02 ± 0.13	B97
	aper. corr.			20.92			
	line cont.			20.99			
6CE1256+3648	literature	-	-	22.23 ± 0.16	I03	22.60 ± 0.16 (4)	I06
	aper. corr.					21.94	
	line cont.			22.29			
6CE1217+3645	literature	22.26 ± 0.32	I03	21.91±0.25	I06	20.59 ± 0.12	I03
	aper. corr.			21.31			
	line cont.	22.26		21.32			
6CE1017+3712	literature	-	-	21.53 ± 0.16	I03	21.10±0.14 (4)	I06
	aper. corr.					20.57	
	line cont.			21.64			
6CE0943+3958	literature	-	-	21.78 ± 0.38	I03	21.55 ± 0.20 (4)	I06
	aper. corr.					20.98	
	line cont.			21.88			
6CE1257+3633	literature	22.04 ± 0.26	I03	21.55 ± 0.30 (4)	I06	20.55 ± 0.12	I03
	aper. corr.			20.98			
	line cont.	22.05		21.00			
6CE1019+3924	literature	21.89 ± 0.25	I03	21.04 ± 0.29 (4)	I06	19.86 ± 0.1	I03
	aper. corr.			20.52			
	line cont.	21.90		20.53			
6CE1011+3632	literature	-	-	21.59 ± 0.19	I03	21.23 ± 0.15 (4)	I06
	aper. corr.					20.69	
	line cont.			21.61			
6CE1129+3710	literature	-	-	21.52 ± 0.14	I03	21.64 ± 0.16 (4)	I06
	aper. corr.					21.06	
	line cont.			21.60			

Table 3. U, B, V, R and I band magnitudes found in the literature. "aper. corr", "line cont.", and "Gal. ext." stand for the magnitude values after being corrected for aperture, emission-line contamination, and Galactic extinction, respectively. An error of 25% was assumed for each magnitude value subjected to any of these corrections. The references to the literature magnitudes are: J01 - Jarvis et al. 2001b; LRL83 - Laing et al. 1983; W98 - Willott et al. 1998; V10 - Vardoulaki et al. 2010

Object	correction	U	Ref	B	Ref	V	Ref	R	Ref	I	Ref
3C280	literature	-	-	-	-	22.00± 1.00	LRL83	21.50±0.50	LRL83	-	-
	line cont.					22.12		21.76			
	Gal. ext.					22.08		21.72			
3C356	literature	-	-	-	-	-	-	21.50±1.00	LRL83	-	-
	line cont.							21.59			
	Gal.ext.							21.50			
3C184	literature	-	-	-	-	-	-	22.00±0.50	LRL83	-	-
	line cont.							22.30			
	Gal. ext.							22.22			
3C175.1	literature	-	-	-	-	-	-	22.00±0.50	LRL83	-	-
	line cont.							22.20			
	Gal. ext.							21.96			
3C22	literature	-	-	-	-	-	-	20.50± 1.00	LRL83	-	-
	line cont.							20.59			
	Gal. Ext.							19.98			
3C289	literature	-	-	-	-	-	-	23.00±0.50	LRL83	-	-
	line cont.							23.42			
	Gal. ext.							23.39			
3C343	literature	-	-	21.06±0.50	LRL83	20.61±0.50	LRL83	19.55±0.50	LRL83	-	-
	line cont.			21.06		20.61		19.55			
	Gal. ext.			20.97		20.54		19.50			
6C*0133+486	literature	-	-	-	-	-	-	23.39 (5)	J01	-	-
	aper. corr.							22.66			
	line cont.							22.72			
5C7.17	literature	-	-	22.08 ± 0.17 (5)	W98	-	-	21.59 ± 0.14	W98	-	-
	aper. corr.			21.88				21.40			
	line cont.			21.89				21.44			
TOOT1267	literature	23.50 ± 0.23	V10	24.60 ± 0.23	V10	24.00 ± 0.23	V10	23.00 ± 0.23	V10	21.70 ± 0.23	V10
	line cont.			24.64		24.03		23.04			
	Gal. ext.	22.20		23.60		23.24		22.40		21.48	
TOOT1140	literature	-	-	-	-	25.20 ± 0.38	V10	22.80 ± 0.38	V10	21.00 ± 0.38	V10
	line cont.					25.22		22.81			
	Gal. ext.					24.93		22.58		20.83	
TOOT1066	literature	-	-	25.30 ± 0.29	V10	24.60 ± 0.05	V10	23.50 ± 0.05	V10	22.50 ± 0.05	-
	line cont.			25.39		24.68		23.58			
	Gal. ext.			24.38		23.91		22.96		22.05	

Table 4. u, g, r, i, z band magnitudes found in the literature. "line cont." and "Gal. ext." stand for the magnitude values after being corrected for emission-line contamination and Galactic extinction, respectively. An error of 25% was assumed for each magnitude value subjected to any of these corrections. The references to the literature magnitudes are: L84 - Lilly & Longair 1984; SDSS - http://www.sdss.org/DR7/access/index.html

Object	correction	u	Ref	g	Ref	r	Ref	i	Ref	z	Ref
3C280	literature	-	-	-	-	21.57 ± 0.07	L84	-	-	-	-
3C356	literature	-	-	-	-	21.84 ± 0.22	L84	-	-	-	-
3C184	literature	-	-	-	-	21.94 ± 0.14	L84	21.14 ± 0.3	L84	-	-
3C175.1	literature	-	-	-	-	21.59 ± 0.15	L84	-	-	-	-
3C289	literature	23.0 ± 0.92	SDSS	23.07 ± 0.32	SDSS	21.65 ± 0.14	SDSS	20.86 ± 0.1	SDSS	20.14 ± 0.2	SDSS
	line cont.			23.19							
	Gal. ext.	22.93		23.15		21.62		20.83		20.12	
6CE1217+3645	literature	23.32 ± 0.64	SDSS	22.77 ± 0.19	SDSS	22.08 ± 0.12	SDSS	21.84 ± 0.15	SDSS	20.77 ± 0.19	SDSS
	line cont.			22.78							
	Gal. ext.	23.23		22.71		22.03		21.80		20.74	
6CE1019+3924	literature	22.66 ± 0.51	SDSS	22.37 ± 0.40	SDSS	21.78 ± 0.15	SDSS	20.37 ± 0.06	SDSS	19.54 ± 0.09	SDSS
	line cont.			22.39							
	Gal. ext.	22.58		22.34		21.74		20.34		19.51	
6CE1011+3632	literature	22.37 ± 0.31	SDSS	23.24 ± 0.23	SDSS	22.25 ± 0.16	SDSS	22.14 ± 0.26	SDSS	21.54 ± 0.46	SDSS
	line cont.			23.26							
	Gal. Ext.	22.30		23.21		22.21		22.11		21.51	